iScience

CellPress
OPEN ACCESS

Article

Multifunctional sponge scaffold loaded with concentrated growth factors for promoting wound healing

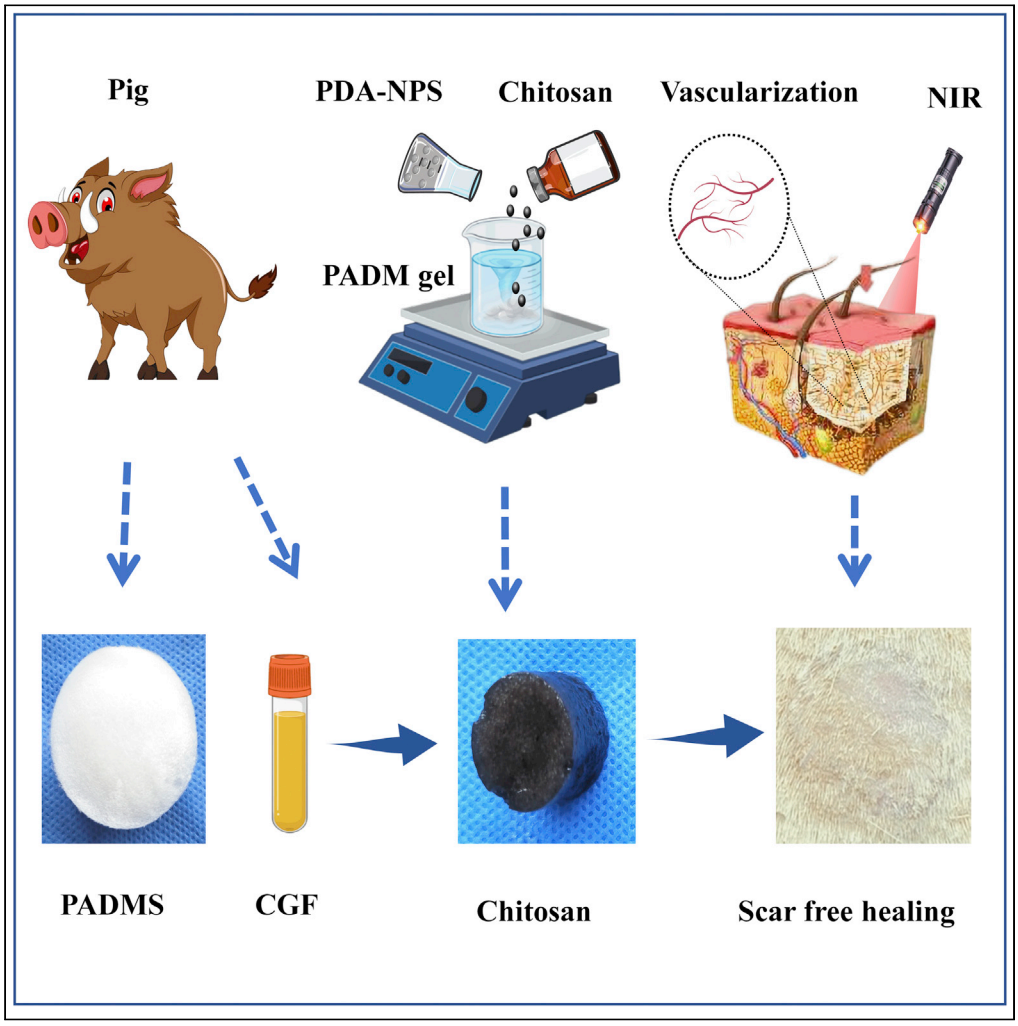

Lianglong Chen, Chaoyang Huang, Yu Zhong, ..., Yanbin Gao, Jun Ma, Lei Yang

gaoyanbin6@yeah.net (Y.G.)
nfyy_majun@163.com (J.M.)
yuanyang@smu.edu.cn (L.Y.)

Highlights

We constructed a multifunctional composite scaffold that can load more CGF

The scaffold has good biocompatibility and photothermal conversion efficiency

The scaffold promotes faster wound healing, better vascularization, and less scar formation

Chen et al., iScience 26, 105835
January 20, 2023
https://doi.org/10.1016/j.isci.2022.105835

iScience

CellPress
OPEN ACCESS

Article

Multifunctional sponge scaffold loaded with concentrated growth factors for promoting wound healing

Lianglong Chen,[1,2] Chaoyang Huang,[1,2] Yu Zhong,[1,2] Yujia Chen,[1] Huihui Zhang,[1] Zijun Zheng,[1] Ziwei Jiang,[1] Xuerong Wei,[1] Yujie Peng,[1] Lei Huang,[1] Libin Niu,[1] Yanbin Gao,[1,*] Jun Ma,[1,*] and Lei Yang[1,3,*]

SUMMARY

Although both are applied in regenerative medicine, acellular dermal matrix (ADM) and concentrated growth factor (CGF) have their respective shortcoming: The functioning of CGF is often hindered by sudden release effects, among other problems, and ADM can only be used in outer dressing for wound healing. In this study, a compound network with physical-chemical double cross-linking was constructed using chemical cross-linking and the intertwining of ADM and chitosan chains under freezing conditions; equipped with good biocompatibility and cell/tissue affinity, the heparin-modified composite scaffold was able to significantly promote cell adhesion and proliferation to achieve adequate fixation and slow down the release of CGF; polydopamine nanoparticles having excellent near-infrared light photothermal conversion ability could significantly promote the survival of rat autologous skin grafts. In a word, this multifunctional composite scaffold is a promising new type of implant biomaterial capable of delivering CGF to promote the healing of full-thickness skin defects.

INTRODUCTION

As the human body's largest organ, skin plays a role in immunity, temperature regulation, and metabolism.[1] Early skin graft or flap transfer is considered an essential treatment for full-thickness skin defects.[2] However, flap transfer therapy involves complicated operations with a high failure rate and may lead to serious donor site injury and scar contracture at the flap site.[3] Despite the good healing effect of skin graft in the early stage, this method inevitably hurts the area providing the skin and cannot ensure sufficient dermal matrix supply for the graft. In the later stage, skin contracture or scar formation often occurs due to uncontrollable scar hyperplasia, reduced mechanical resistance, and other shortcomings, seriously affecting the appearance and function of the treated site. Therefore, preventing severe scar hyperplasia and contracture in the later stage remains a crucial challenge for skin grafting.

As the third-generation platelet-rich preparation, concentrated growth factor (CGF) has a mature production process and is widely applied in clinical practices. It stands out for its high platelet concentration, which is 5–-6 times higher than that of whole blood platelet, and for its ability to release much more growth factors (GFs) to effectively stimulate cell proliferation and differentiation and boost tissue restoration.[4] Prepared by centrifuging blood samples, CGF is simple to produce, low in cost, and less harmful to the body. Various GFs are involved in the platelet concentrate function independently but coordinately to jointly promote wound healing and provide a wound bed microenvironment suitable for granulation tissue growth and epithelial crawling.[5] However, although the secreted GFs stimulate angiogenesis and the proliferation and migration of skin-related cells, the sudden and rapid release process inevitably leads to the waste of many GFs.[6] Therefore, how to release GFs slowly and minimize waste is a major issue to be addressed.

An artificial dermis substitute (referred to as an artificial dermis) is a double-layer scaffold material composed of collagen, polysaccharide, extracellular matrix, among other substances, and a medical silica gel layer.[7] It functions by stimulating the proliferation, migration, and adhesion of skin-related cells through the activity of the material itself to promote wound healing. Approved products include Lando from China, Integra from the United States, and Pelnac from Japan.[8,9] This product is essentially a collagen sponge scaffold having a three-dimensional porous structure, which can reduce skin contractures and the

[1]Department of Burns, Nanfang Hospital, Southern Medical University, Jingxi Street, Baiyun District, Guangzhou 510515, P.R. China

[2]These authors contributed equally

[3]Lead contact

*Correspondence: gaoyanbin6@yeah.net (Y.G.), nfyy_majun@163.com (J.M.), yuanyang@smu.edu.cn (L.Y.)

https://doi.org/10.1016/j.isci.2022.105835

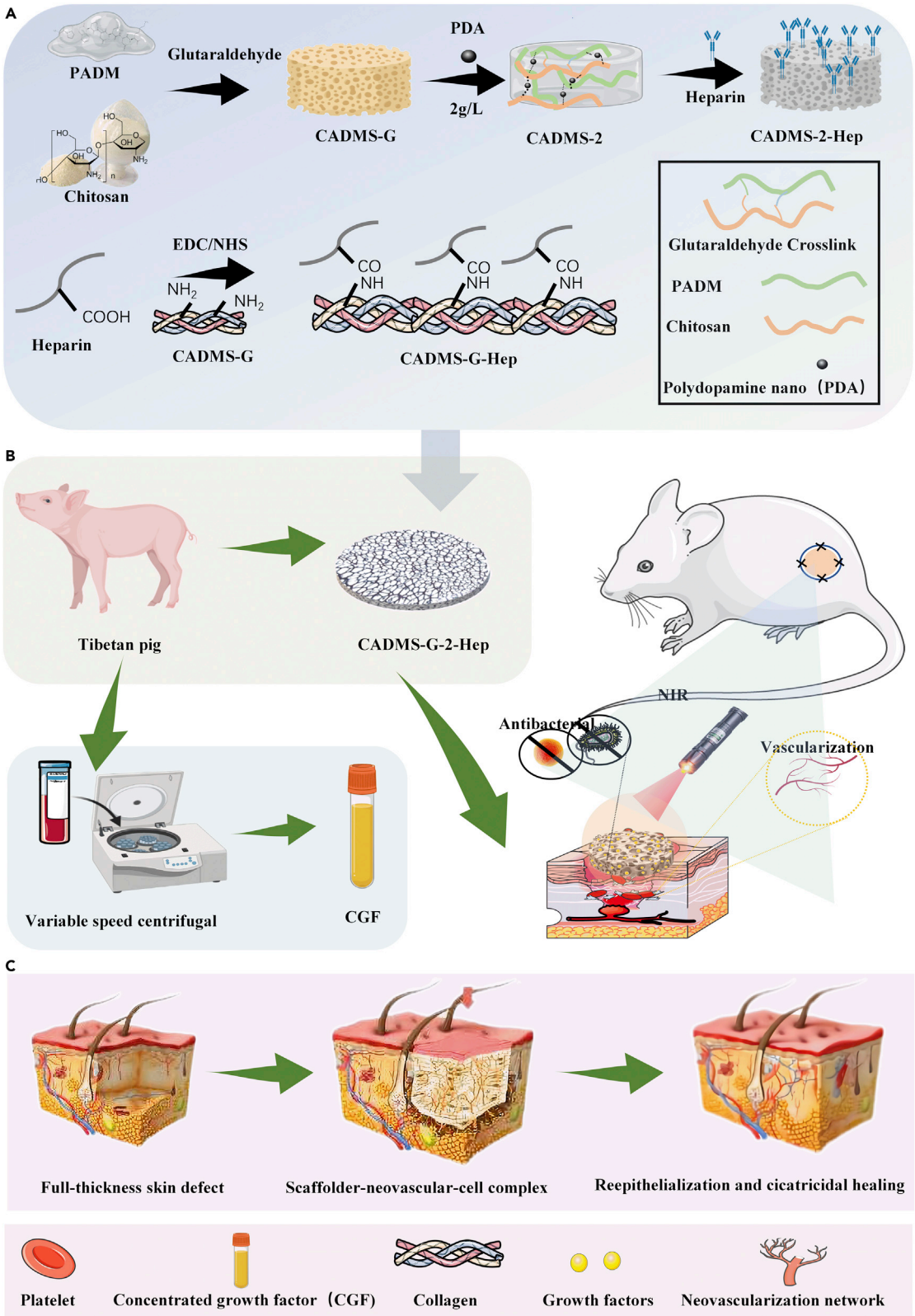
A
PADM
Glutaraldehyde
CADMS-G
PDA
2g/L
CADMS-2
Heparin
CADMS-2-Hep
Chitosan
EDC/NHS
COOH
Heparin
NH2
NH2
CADMS-G
CO
NH
CADMS-G-Hep
Glutaraldehyde Crosslink
PADM
Chitosan
Polydopamine nano (PDA)
B
Tibetan pig
CADMS-G-2-Hep
NIR
Antibacterial
Vascularization
Variable speed centrifugal
CGF
C
Full-thickness skin defect
Scaffolder-neovascular-cell complex
Reepithelialization and cicatricidal healing
Platelet
Concentrated growth factor (CGF)
Collagen
Growth factors
Neovascularization network

Figure 1. Schematic diagram of the preparation of multifunctional dermal repair scaffold

(A) Schematic diagram of the CADMS-G-2-Hep preparation process.

(B) CGF immobilized CADMS-G-2-Hep composite scaffold synergistically accelerated wound healing under NIR stimulation.

(C) Schematic diagram of one-step composite scaffold combined with autologous skin graft to reduce scarring.

formation of scars, restore the appearance and function of the defective skin, and minimize damage to the skin-providing area.[10] However, using artificial dermis in the treatment of skin and soft tissue defects is often faced with the following problems[11,12]: (1) Permanent skin transplantation is essential for repairing soft tissue defects, but the artificial dermis cannot effectively promote skin graft angiogenesis due to wound ischemia; (2) although artificial dermis scaffold serves as skin regeneration templates, its poor mechanical properties mean it cannot maintain the microstructure after implantation, and repeated skin grafting is required because the scaffold will shrink severely after the second stage; and (3) lacking diversity in components and functions, the artificial dermal scaffold cannot provide enough extracellular matrix for re-epithelialization, and there is a risk of infection in the later stages of skin transplantation.

Porcine acellular dermal matrix (ADM) is a dermal substitute made of heterogeneous skin. The preparation of this biomaterial involves the removal of cellular compositions other than the dermal extracellular matrix in the skin through physical or chemical methods to retain good biocompatibility. Resembling human skin in the composition and immunological aspects, ADM has been used in wound repair over the years.[13] Still, the ADM implant in a defective wound cannot maintain an effective nutrition supply that the skin graft needs to regenerate sufficient new blood vessels, making it extremely time-consuming for new blood vessels to reach the dermis. These factors may cause the skin-related cells to proliferate too slowly that the skin graft becomes necrotic and eventually sheds.[14,15] Therefore, improving the permeability and porosity of ADM is the key to enhancing the transplantation survival rate.

In recent years, mussel-inspired Polydopamine nanospheres (PDA-NPS) have received extensive attention from researchers due to their high photothermal conversion efficiency.[16] Most importantly, as the main component of melanin, polydopamine (PDA) exhibits excellent biocompatibility and high tissue affinity, making it a material of choice for promoting cell adhesion and proliferation.[17] Moreover, PDA-NPS can easily form chemical bonds with thiol or amine groups, favoring its better distribution and entanglement in the polymer network. Therefore, PDA-NPS can be incorporated into the network structure of natural polymer materials to jointly form a skin substitute with excellent near-infrared (NIR) photothermal properties for promoting wound healing.[18]

This study incorporated PDA-NPS into the ADM-chitosan (CS) interpenetrating network structure. We modified it through heparinization and prepared a drug delivery composite scaffold that has NIR photothermal responsiveness. The antibacterial activity, NIR photothermal conversion ability, and effects on the composite scaffolds' CGF fixation and release behaviors were evaluated. Finally, the results of NIR photothermal therapy, CGF-promoting graft survival, and their synergistic effects on skin tissue regeneration in the full-thickness defect wound of rats were investigated in combination with one-step autologous skin transplantation.

RESULTS AND DISCUSSION

Preparation and characterization of an ADM gel

Wound healing involves many intricate physiological processes.[19] As a result, multifunctional implantable scaffold materials with an enhanced biochemical process of wound healing have been attracting much attention. The synthesis principle of multifunctional scaffold materials is shown in Figure 1. Polydopamine nanospheres (PDA-NPS) with excellent NIR photothermal conversion ability were doped into the interpenetrating network structure of ADM glue and CS, and the sponge scaffold was modified with heparin (Chitosan mixed acellular dermal matrix-glutaraldehyde crosslinking- heparinization modification, CADMS-G-Hep). Thus, a multifunctional composite sponge scaffold with good NIR photothermal responsiveness, antibacterial activity, and drug delivery ability was prepared (Figures 1A and 1B). With excellent photothermal conversion ability, PDA-NPS can improve the survival of autologous skin grafts in rats while reducing skin shrinkage and scar formation (Figure 1C).

The hypertonic salt alkali method was adopted to prepare the ADM in the early stage.[20] The prepared ADM was cut into pieces and then stirred and dissolved in acetic acid solutions of different concentrations to

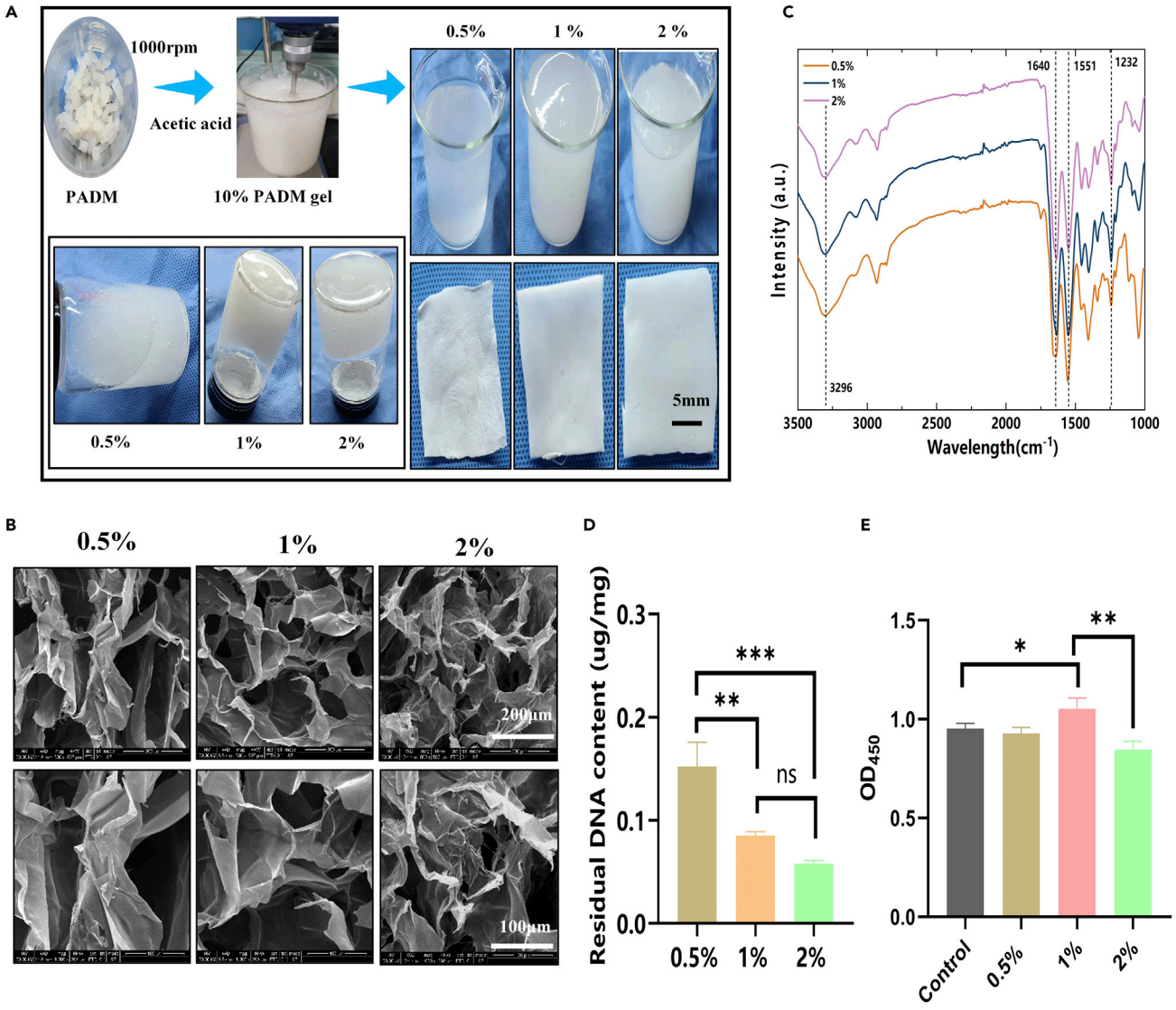

Figure 2. Preparation and characterization of ADM gel

(A) Images of ADM dissolved in acetic acid at varying concentrations (0.5%, 1%, 2%) before and after lyophilization.

(B) SEM images of ADM sponges.

(C) FTIR spectra of 0.5%, 1%, and 2% groups.

(D) Residual DNA contents in 0.5%, 1%, and 2% groups.

(E) Evaluation of cytotoxicity of ADM sponges by CCK-8. (*$p < 0.05$, **$p < 0.01$, ***$p < 0.001$).

obtain the ADM glue. As shown in Figure 2A, the ADM glue became more viscous with the increase in acetic acid concentration. We speculate that with the increase of acetic acid concentration, the ADM dissolved more completely, collagen molecules tended to form larger aggregates, and matrix proteins intertwined and aggregated, so the solution showed significant viscoelastic behavior.[21] Scanning electron microscopy (SEM) images (Figure 2B) show that the ADM gel developed a white porous structure after freeze-drying. Compared with other groups, the ADM prepared with 1% acetic acid exhibited a continuous and interlaced sponge structure that was more orderly and looser. A structure such as this helps transport nutrients, cell migration, and angiogenesis in the body. The inner wall and surface of the ADM pore prepared by 1% acetic acid were also flatter, which could facilitate cell attachment and growth.[22] Figure S1 shows the material's Raman spectrum, where the peak intensities of proline (near 856 cm^{-1}) and elastin (near 1,126 cm^{-1}) can be seen. The amide I and III bands appear near 1,644 cm^{-1} and 1,322 cm^{-1}, respectively. A prominent absorption peak between the amide I and III bands indicated the existence of a helical structure in the sample. The

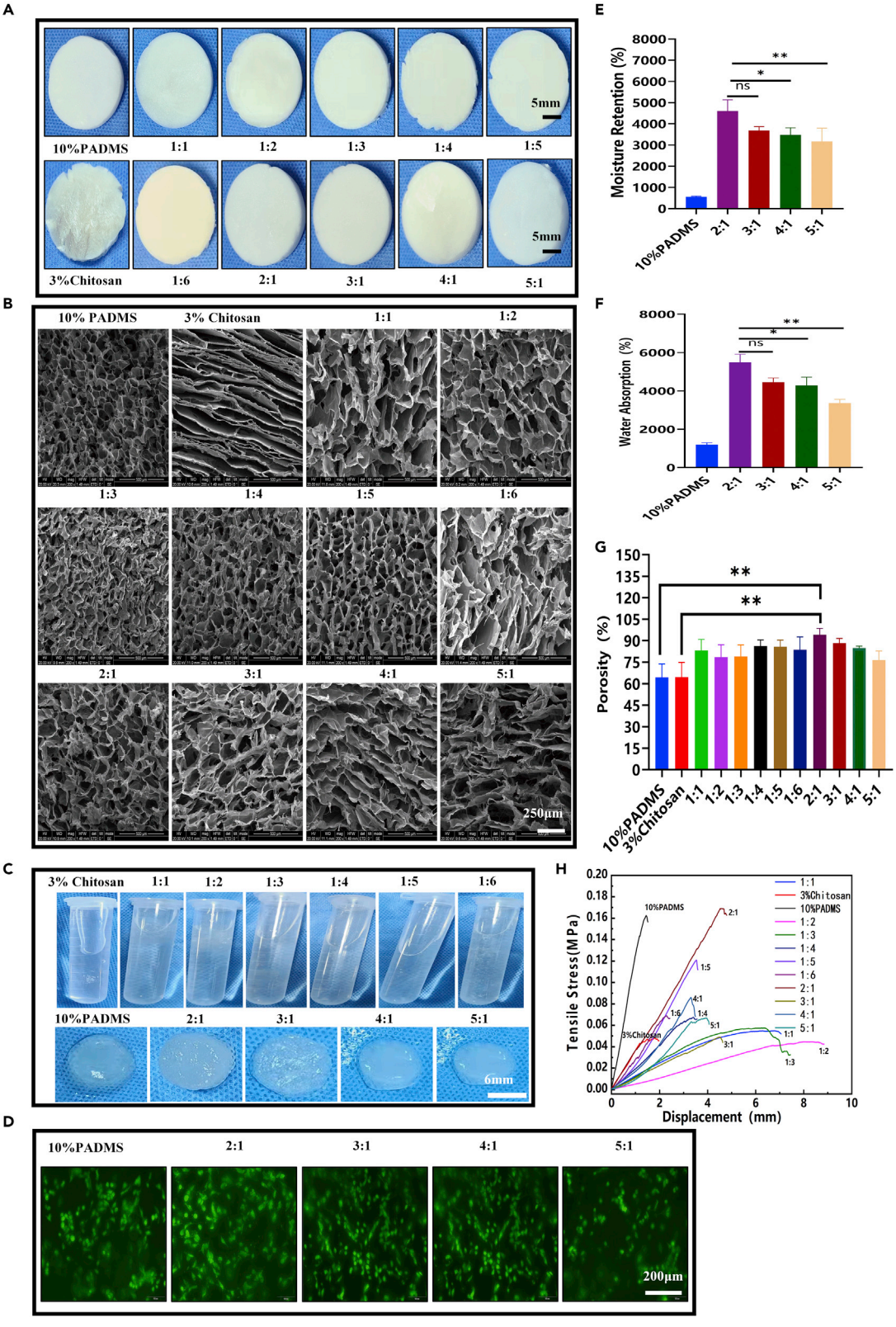
A
10%PADMS
1:1
1:2
1:3
1:4
1:5
5mm
3%Chitosan
1:6
2:1
3:1
4:1
5:1
5mm
B
10% PADMS
3% Chitosan
1:1
1:2
1:3
1:4
1:5
1:6
2:1
3:1
4:1
5:1
250μm
C
3% Chitosan
1:1
1:2
1:3
1:4
1:5
1:6
10%PADMS
2:1
3:1
4:1
5:1
6mm
D
10%PADMS
2:1
3:1
4:1
5:1
200μm
E
Moisture Retention (%)
8000
7000
6000
5000
4000
3000
2000
1000
0
**
*
ns
10%PADMS
2:1
3:1
4:1
5:1
F
Water Absorption (%)
8000
6000
4000
2000
0
**
*
ns
10%PADMS
2:1
3:1
4:1
5:1
G
Porosity (%)
150
135
120
105
90
75
60
45
30
15
0
**
**
10%PADMS
3%Chitosan
1:1
1:2
1:3
1:4
1:5
1:6
2:1
3:1
4:1
5:1
H
Tensile Stress(MPa)
0.20
0.18
0.16
0.14
0.12
0.10
0.08
0.06
0.04
0.02
0.00
0
2
4
6
8
10
Displacement (mm)
10%PADMS
3%Chitosan
1:1
3%Chitosan
10%PADMS
1:2
1:3
1:4
1:5
1:6
2:1
3:1
4:1
5:1

Figure 3. Preparation and characterization of ADM-CS composite sponge scaffolds

(A) Freeze-dried morphology of 10% PADM mixed with 3% CS at different volume ratios.

(B) SEM images of PADM-CS.

(C) Morphology of PADM-CS soaking in deionized water.

(D) Evaluation of biocompatibility of various materials in PADM-CS groups by living and dead cell staining.

(E) Determination of moisture retention of the materials.

(F) Determination of water absorption of the materials.

(G) Determination of material porosity.

(H) Tension–stress curves of the materials (*$p < 0.05$, **$p < 0.01$, ***$p < 0.001$).

above results suggested that the three-dimensional structure of collagen in Porcine acellular dermal matrix sponge (PADMS) was intact. Figure 2D shows that sponge DNA content gradually decreased with the increase of acetic acid concentration, which was 0.15 $\pm$ 0.02 μg/mg, 0.09 $\pm$ 0 μg/mg, and 0.06 $\pm$ 0 μg/mg. The Cell Counting Kit-8 (CCK-8) assay was used to evaluate the cytotoxicity of the materials. Figure 2E shows that the ADM prepared with 1% acetic acid had good biocompatibility, while excessively high concentrations of acetic acid (2%) caused damage to cells. Therefore, ADM adhesive prepared at 1% concentration was selected for subsequent experiments.

Preparation and characterization of CAMDS composite sponge scaffolds

The superficial characteristics of these composite sponges were observed at macro and micro levels, as shown in Figure 3A. With the increase in the proportion of CS, the color of composite sponges gradually turned from white to light yellow with uniform distribution, indicating that CS was evenly dispersed.[23,24] The SEM results in Figure 3B show that the pure CS sponge was layered, and the composite scaffold had a porous sponge-like structure and a continuous radiative arrangement. The inner wall of the hole had a flat surface, which is conducive to cell attachment and growth. PADM-CS composite sponges (CADMS) were soaked in deionized water (Figure 3C). Only the 10% PADM and the 2:1, 3:1, 4:1, and 5:1 groups absorbed water and swelled in fixed shapes, while the other groups dissolved in the water. The staining results of living and dead cells (Figure 3D) showed that each group had good biocompatibility and that cells adhered along the pore structure of the sponge. The sponge scaffold has a strong water absorption capacity and can absorb the exudate from the wound to prevent fluid accumulation between the sponge and the wound. It can also promote the average growth of granulation and epithelial tissue and accelerate wound healing. The moisturizing performance of sponge scaffold is mainly reflected in that it can adhere to the wound evenly and tightly, prevent the loss of body fluid and water, improve microcirculation, and effectively enhance the wetness of the wound microenvironment.[25] Figures 3E and 3F show that the 2:1 group composite sponge had a good capacity for water absorption (5,480.74 $\pm$ 430.14%) and moisture retention (4,604.06 $\pm$ 528.87%). Therefore, adding a certain amount of CS to the PADM sponge can improve moisture retention and water absorption performance. It is well known that sponges' pore structure and porosity are vital factors affecting wound healing because they have a significant impact on the absorption of blood and exudates.[26] The pore structure of the composite sponge was measured by the ethanol replacement method. As shown in Figure 3G, the 2:1 group had excellent porosity (94.1 $\pm$ 4.52%), which indicated that adding an appropriate proportion of CS could improve the composite sponge's physical and chemical properties. Figure 3H further verifies the above conclusions from the mechanical perspective. In summary, composite sponges in the 2:1 group were selected for subsequent experiments and redefined as the CADMS group.

Glutaraldehyde cross-linking and heparinization modification of composite sponge scaffold

According to the literature,[27,28] 0.02 V/V.% glutaraldehyde was selected to perform appropriate cross-linking of the material. As shown in Masson's trichrome staining and hematoxylin and eosin (H&E) staining results in Figure 4A, no residual nuclei were found in the composite sponge, and the collagen was well preserved. In the Chitosan mixed acellular dermal matrix scaffold (CADMS) group, the staining of Masson was light. We assumed that adding CS made the collagen distribute more sparsely and that CS could also retain some of the Masson staining reagent. As shown in Figure 4B, after glutaraldehyde cross-linking, the SEM image of the cross-linked composite sponge was similar to that of the unmodified collagen sponge, indicating that glutaraldehyde cross-linking had no noticeable effect on the porous microstructure. However, other changes in pore size and shape could be observed at a higher magnification. The composite sponge cross-linked with glutaraldehyde had a large number of interconnected micropores. These pores' inner walls were flatter, suitable for cell penetration, and conducive to wound exudate absorption, oxygen supply, and cell proliferation.[29,30] As shown in the infrared spectra of the sponge scaffold (Figure 4C), where

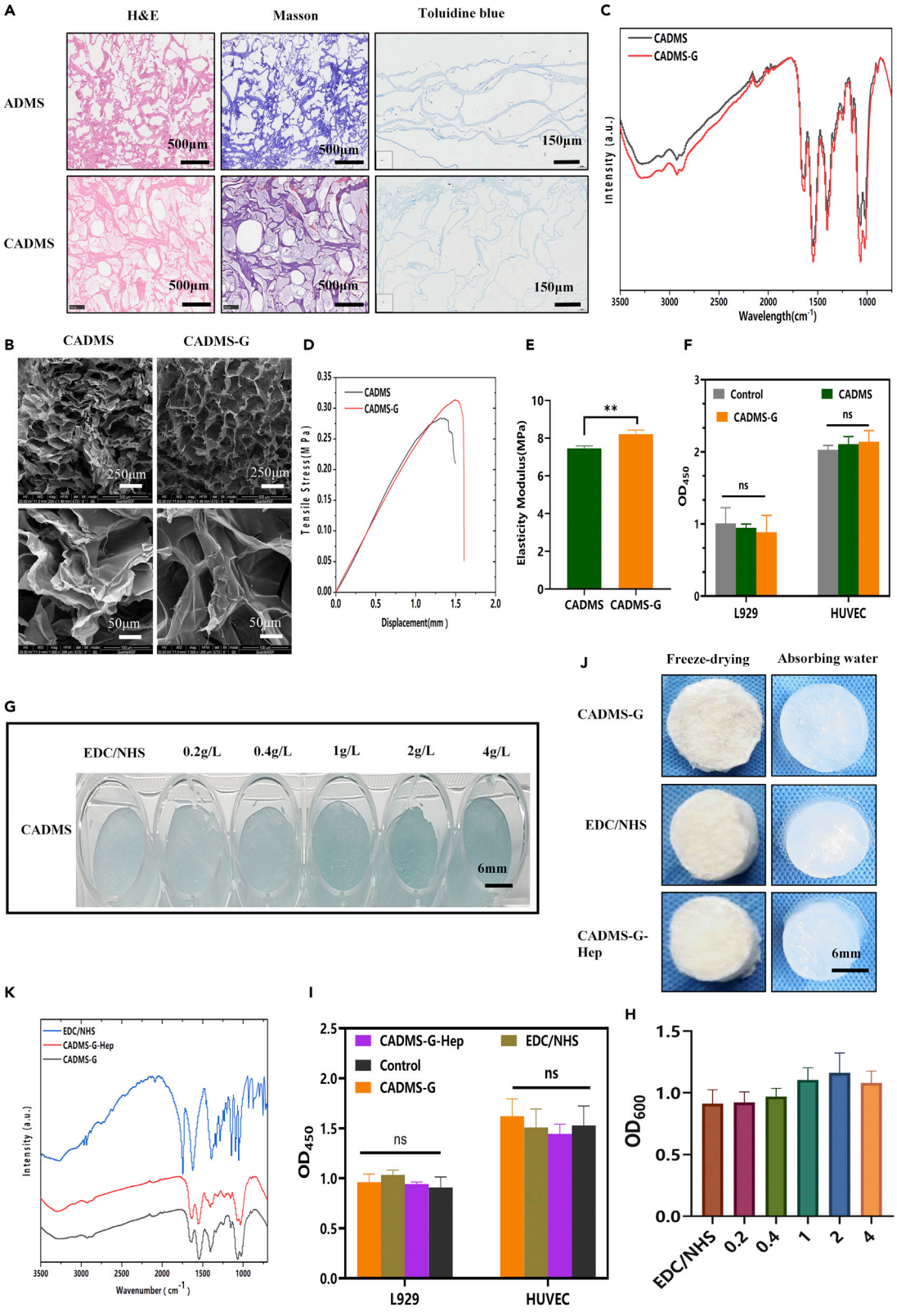
A
H&E
Masson
Toluidine blue
ADMS
CADMS
500μm
150μm
C
CADMS
CADMS-G
Intensity (a.u.)
Wavelength(cm-1)
B
CADMS
CADMS-G
250μm
50μm
D
Tensile Stress(MPa)
Displacement(mm)
E
Elasticity Modulus(MPa)
**
CADMS
CADMS-G
F
Control
CADMS
CADMS-G
ns
OD450
L929
HUVEC
G
EDC/NHS
0.2g/L
0.4g/L
1g/L
2g/L
4g/L
CADMS
6mm
J
Freeze-drying
Absorbing water
CADMS-G
EDC/NHS
CADMS-G-Hep
6mm
K
EDC/NHS
CADMS-G-Hep
CADMS-G
Intensity (a.u.)
Wavenumber (cm-1)
I
CADMS-G-Hep
EDC/NHS
Control
CADMS-G
ns
OD450
L929
HUVEC
H
OD600
EDC/NHS
0.2
0.4
1
2
4

Figure 4. Glutaraldehyde cross-linking and heparinization of composite sponge scaffolds

(A) CADMS's and ADM's H&E staining, Masson's trichromatic and toluidine blue staining.
(B) SEM images before and after glutaraldehyde cross-linking.
(C) Fourier infrared spectra of glutaraldehyde before and after cross-linking.
(D) Tensile stress curves.
(E) Elastic modulus.
(F) Relative cell viability before and after glutaraldehyde cross-linking.
(G) Toluidine blue staining after heparinized modification.
(H) Determined absorbance of toluidine blue at OD^{600}.
(I) Relative cell viability before and after heparin sodium modification.
(J) Changes of CADMS-G hygroscopicity before and after heparinization.
(K) Fourier infrared spectroscopy before and after heparinization.

the characteristic peak of the collagen/CS scaffold is displayed, there were several absorption bands of the CS polysaccharide structure at 1,645 cm^{-1} (C=O stretched in the amide I), 1,550 cm^{-1} (N–H bent in amide II), and 1,151 cm^{-1} (C–O–C).[31] The cross-linked glutaraldehyde scaffold had an additional peak at 1, 652 cm^{-1} (C=N bond), indicating the presence of a Schiff base in glutaraldehyde (GTA).[32] Representative stress-strain curves before and after glutaraldehyde cross-linking are shown in Figure 4D. The elastic modulus of scaffolds was calculated according to the stress-strain curves (Figure 4E). Glutaraldehyde cross-linking increased the tensile strain at the fracture of materials in the CADMS group but did not significantly increase the elastic modulus of materials (normal saline [NS], $p > 0.05$). CCK-8 assay (Figure 4F) confirmed that appropriate glutaraldehyde cross-linking occurred in a noncytotoxic manner ($p > 0.05$).

Many GFs bind to heparin and cell surface heparan sulfate proteoglycan (HSPG) to form stably activated GF–fibroblast GF receptor complexes so that these GFs can maintain their biological activity while being released slower. Such GFs are known as heparin-affinity GFs, including fibroblast GFs, vascular endothelial GFs (VEGF), hepatocyte GF, and transforming GF β (TGF-β).[33] The most widely used and mature method is the spectrophotometric determination of trace heparin using toluidine blue.[34] As can be seen from Figures 4G and 4H, the toluidine blue color gradually darkened with the increase of heparin concentration (0.2 g/L, 0.4 g/L, 1 g/L, 2 g/L, and 4 g/L). Absorbance reached the peak when the heparin concentration was 2 g/L, suggesting that the modification of heparin reached saturation. It can be seen from the infrared spectra (Figure 4K) that the characteristic peaks of OSO_3^- and SO_3^- on heparin are located at 1, 224 cm^{-1} and 1,143 cm^{-1}, respectively, indicating that heparin had been effectively bound to the composite scaffold of CADMS-G. Figure 4J shows no significant change in the morphology of CADMS-G before and after heparinization modification. CCK-8 test confirmed that heparinized conversion had no significant effect on cell proliferation (Figure 4I) (NS, $p > 0.05$).

Preparation and characterization of composite sponge scaffolds doped with PDA-NPS

PDA-NPS can be incorporated into the network structure of natural polymer materials as an NIR photothermal material to form skin substitutes with good photothermal properties for wound healing.[35] Figure 5A illustrates the preparation process of PDA-NPS. Figure 5B shows that the colorless, transparent solution gradually changed to a light brown one as the reaction went on. After 24 h of reaction, the color of the solution was brown-black without further changes, indicating the completion of polymerization. The ultraviolet (UV) spectra (Figure 5C) show that the solution had a strong absorption peak at 280 nm, which was the characteristic UV absorption peak of a dopamine monomer. As the reaction progressed, the absorption peak of the solution at 280 nm gradually weakened, while the absorption peak at 320 nm appeared, indicating the formation of quinone bonds. The absorption peak at 370 nm suggested intramolecular cyclization between quinone bond derivatives, indicating PDA formation.[36] A SEM image (Figure 5D) showed that the average particle size of the prepared PDA-NPS was about 0.17 ± 0.02 μm, with uniform particle size distribution.

As shown in Figure 5E, CADMS-G gradually darkened in color with increased PDA-NPS concentration. At 2 g/L, CADMS-G showed homogeneous black and formed a black spongy shape after freeze-drying. Through SEM (Figure 5F), it was observed that after adding PDA-NPS, the composite scaffold retained a similar interpenetrating three-dimensional porous structure as the CADMS-G scaffold. PDA-NPS in the 2-g/L groups were evenly dispersed and embedded in the pore wall of the composite scaffold, while aggregation occurred in the 4-g/L group. CCK-8 results (Figure 5G) confirmed that the incorporation of PDA-NPS occurred in a noncytotoxic manner. The PDA-NPS surface contains many hydrophilic groups,[37] so it is

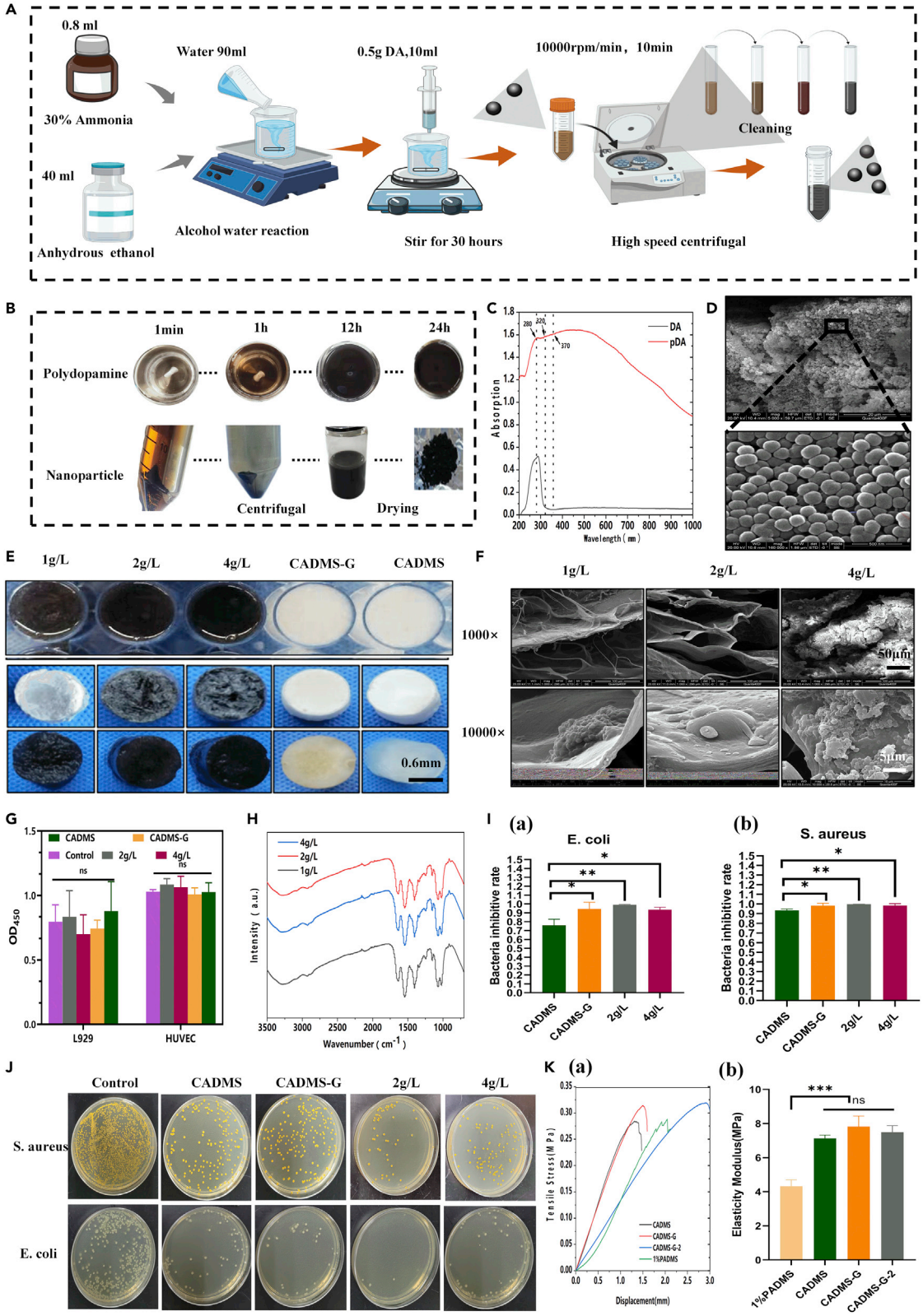
A
0.8 ml
30% Ammonia
40 ml
Anhydrous ethanol
Water 90ml
Alcohol water reaction
0.5g DA,10ml
Stir for 30 hours
10000rpm/min，10min
Cleaning
High speed centrifugal
B
1min
1h
12h
24h
Polydopamine
Nanoparticle
Centrifugal
Drying
C
DA
pDA
Absorption
Wavelength (nm)
D
E
1g/L
2g/L
4g/L
CADMS-G
CADMS
0.6mm
F
1g/L
2g/L
4g/L
1000×
10000×
50μm
5μm
G
CADMS
CADMS-G
Control
2g/L
4g/L
ns
OD450
L929
HUVEC
H
4g/L
2g/L
1g/L
Intensity (a.u.)
Wavenumber (cm-1)
I
(a)
E. coli
Bacteria inhibitive rate
CADMS
CADMS-G
2g/L
4g/L
(b)
S. aureus
J
Control
CADMS
CADMS-G
2g/L
4g/L
S. aureus
E. coli
K
(a)
Tensile Stress(MPa)
Displacement(mm)
CADMS
CADMS-G
CADMS-G-2
1%PADMS
(b)
Elasticity Modulus(MPa)
***
ns
1%PADMS
CADMS
CADMS-G
CADMS-G-2

Figure 5. Preparation and characterization of the composite sponge scaffold doped with PDA-NPS

(A) PDA-NPS preparation process model diagram.
(B) PDA-NPS synthesis process.
(C) UV spectra of PDA-NPS.
(D) SEM images of PDA-NPS.
(E) The freeze-desiccation-wetting process of the sponge scaffold doped with PDA-NPS.
(F) SEM images of dopamine nanospheres composite sponge.
(G) Relative cell viability.
(H) Fourier infrared spectroscopy.
(I) Antibacterial rates of *Escherichia coli* (a) and *Staphylococcus aureus* (b).
(J) Photographs of *in vitro* antibacterial experiments by AGAR dilution method.
(K) The (a) stress-strain curves and (b) elastic modulus of the material obtained through the tensile test (*$p < 0.05$, **$p < 0.01$, ***$p < 0.001$).

supposed to interact well with –OH in the CADMS-G molecular chain. The comparison of Fourier infrared absorption spectra (Figure 5H) showed that the composite scaffold with PDA-NPS had stronger –OH stretching vibration peaks near 3,274 cm^{-1} and 1,086 cm^{-1}. The movement of these –OH peaks indicated the strong hydrogen bonding between PDA-NPS and CADMS-G.

The influential group NH_3^+ of CS can react with lipids and protein complexes on bacterial cell membranes to denature proteins, change cell membrane permeability, and damage cell wall integrity, playing a bactericidal and bacteriostatic role.[38] The antibacterial capacity of the composite sponge against *Escherichia coli* (gram-negative) and *Staphylococcus aureus* (gram-positive) was studied by the colony-forming unit test.[39] The qualitative images (Figure 5J) show that the relationship of the antibacterial rates among the test groups was 2-g/L group > CADMS-G group > 4-g/L group. As shown in Figure 5I, the relative inhibition rate of *S. aureus* in each group was 1 $\pm$ 0, 0.99 $\pm$ 0.02, and 0.98 $\pm$ 0.02, respectively, and the comparable inhibition rate of *E. coli* in each group was 0.99 $\pm$ 0, 0.94 $\pm$ 0.08, and 0.93 $\pm$ 0.03, respectively. The mechanical properties test (Figure 5K) showed that adding PDA-NPS increased the tensile strain at the fracture of the material but did not significantly improve the material's elastic modulus.

Because PDA-NPS can efficiently convert NIR light into heat, PDA-doped composite scaffolds are a potentially ideal material for photothermal therapy.[40] The composite scaffold was soaked in distilled water and irradiated with the 808-nm NIR laser (0.8 W cm^{-2}). The temperature of the distilled water was measured and recorded at specific time intervals. As shown in Figures 6A and 6B, the NIR photothermal conversion of the composite scaffold depended on the content of PDA-NPS in the composite scaffold, specifically, the higher the PDA-NPS content was in the composite scaffold, the higher the temperature increased. After 30 min of NIR laser irradiation, the water temperature around the composite scaffold in the 2-g/L group increased slowly from 22°C to 44°C while the temperature in the 4-g/L group reached 47°C due to the local accumulation of PDA-NPS (Figure 6C). Mild local fever of wound surface (41°C–43°C) can induce the proliferation of vascular endothelial cells, effectively increasing the vascular density of new granulation tissue, promoting collagen deposition, hair follicle regeneration, fibroblast proliferation, and accelerating tissue healing. Moderate fever (45°C–50°C) can quickly cause negligible damage to normal tissue cells and fatal damage to the tumor tissue. For the healing of infected wounds, hyperthermia (>50°C) can effectively inhibit bacterial proliferation.[35,41] Therefore, the photothermal effect of a composite sponge scaffold should be controlled within a suitable range. In this experiment, the 2-g/L group was selected for subsequent experiments and renamed as CADMS-G-2-Hep.

The acellular matrix is mainly composed of different types of collagens. It also contains a small amount of fiber-connective proteins, laminin, and so on. The *in vivo* degradation process of this material is a key factor affecting its application as an implant scaffold material.[42] After *in vivo* implantation, the mechanical strength will drop so quickly that the fibroblasts will not have enough time to produce qualified extracellular matrix for the autologous tissue; if the degradation is too slow, the regeneration and restoration of tissues will be affected, triggering immune reactions such as rejection and encapsulation.[43] Therefore, studying the *in vivo* degradation process of collagen-based biomaterials is of great significance for improving the coordination between the degradation process and the autologous tissue formation of the receptor. *In vitro* degradation test results (Figure 6D) showed that the CADMS-G-Hep group and CADMS-G-2-Hep group still had residues after 24 h, while no visible residues were observed in the control group. Their 28-h degradation rates were 0.89 $\pm$ 0.02, 0.91 $\pm$ 0.02, and 0.75 $\pm$ 0.03, respectively (Figure 6E). *In vivo* degradation experiment results (Figures 6F and 6G) showed that precise contours could be seen in each group after 2 weeks, with a parcel formation between the material and the tissue and

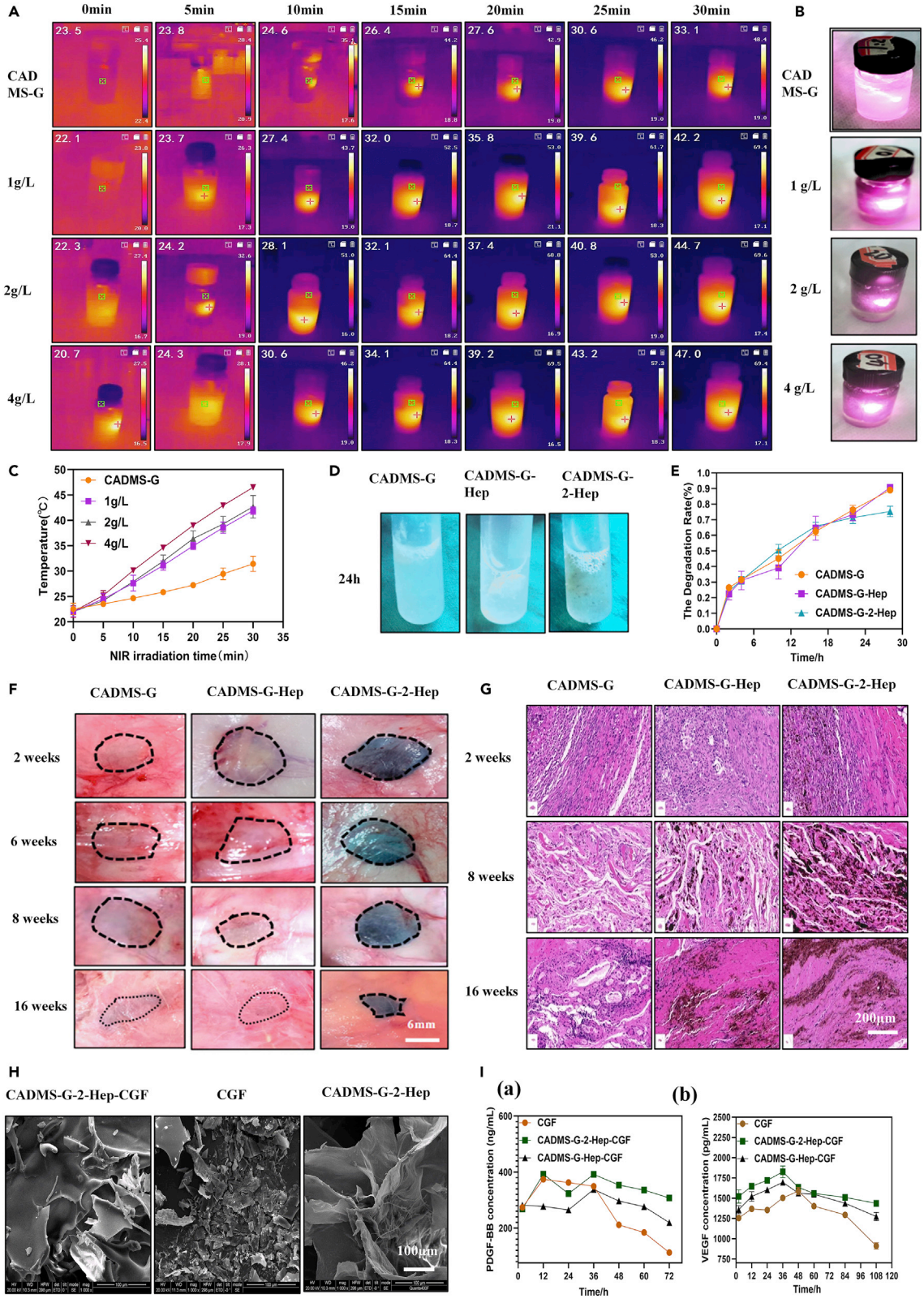
A
0min
5min
10min
15min
20min
25min
30min
CAD
MS-G
1g/L
2g/L
4g/L
B
CAD
MS-G
1 g/L
2 g/L
4 g/L
C
CADMS-G
1g/L
2g/L
4g/L
Temperature(℃)
NIR irradiation time (min)
D
CADMS-G
CADMS-G-Hep
CADMS-G-2-Hep
24h
E
The Degradation Rate(%)
CADMS-G
CADMS-G-Hep
CADMS-G-2-Hep
Time/h
F
CADMS-G
CADMS-G-Hep
CADMS-G-2-Hep
2 weeks
6 weeks
8 weeks
16 weeks
6mm
G
CADMS-G
CADMS-G-Hep
CADMS-G-2-Hep
2 weeks
8 weeks
16 weeks
200μm
H
CADMS-G-2-Hep-CGF
CGF
CADMS-G-2-Hep
100μm
I
(a)
(b)
CGF
CADMS-G-2-Hep-CGF
CADMS-G-Hep-CGF
PDGF-BB concentration (ng/mL)
VEGF concentration (pg/mL)
Time/h
Time/h

Figure 6. Construction and characterization of the composite sponge doped with PDA-NPS and its drug delivery system

(A) Photothermal images of various composite scaffolds under 808-nm NIR laser irradiation.

(B) The physical images of the NIR photothermal performance of composite scaffolds.

(C) The temperature changes of the composite scaffold under 808-nm NIR laser irradiation.

(D) The physical images of the 24-h *in vitro* composite scaffold collagenase degradation experiment.

(E) Dynamic quantitative statistical chart of *in vitro* degradation experiments.

(F) Images illustrating subcutaneous degradation of composite scaffold implants in rats.

(G) Images illustrating the *in vivo* degradation of H&E staining at different time points.

(H) SEM images of drug-delivered stents.

(I) Growth factor release assay of *in vitro* drug-delivered stents: (a) PDGF-BB; (b) VEGF.

evident inflammatory cell infiltration reaction around the tissue. Materials in the CADMS-G group and CADMS-G-Hep group were completely degraded at week 16, and the location of materials could only be roughly determined. However, materials in the CADMS-G-2-Hep group had irregular shapes and were completely attached to tissue fascia, making it difficult for total separation. The undegraded part was thin and dense, without any noticeable infiltration of inflammatory cells.

Many attempts have been made to increase the stability of GFs through heparin binding, which can be used as an initial binding site for GFs in the extracellular matrix until they are released to function at the cellular level.[44] The microstructure (Figure 6H) showed that fibrin fragments in the CADMS-G-2-Hep group remained in the pores of the composite scaffold after loading CGF. Results of the *in vitro* GF release experiment (Figure 6J) showed explosive release of Platelet derived growth factor (PDGF-BB) and Vascular endothelial growth factor (VEGF) within 36 h in the CGF-alone group. The sudden release effect of the CADMS-G-Hep group was alleviated to some extent, while the release of GFs was the slowest and steadiest in the CADMS-G-2-Hep group, which may be due to the abundant functional groups of PDA-NPS as bioactive sites for adequate fixation and slow release of GFs.[36,45]

Cell migration experiment

Wound healing involves multiple processes including cell proliferation, migration, and angiogenesis. An improved cell migration experiment was conducted to reflect the characteristics of wound healing and tissue regeneration.[20] As shown in Figure 7A, the transwell chamber was placed above the adherent cells, and the material was placed in the chamber and submerged in the cell culture medium.[45] At 36 h after scratches, both in human umbilical vein endothelial cells (HUVEC) and L929 cells, cells from both sides of the CADMS-G-2-Hep-CGF and CADMS-G-4-Hep-CGF groups had been in contact (Figures 7D and 7E), showing significantly increased mobility (Figures 7B and 7C). The results showed that the CADMS-G-Hep-CGF group significantly promoted cell migration within 36 h ($p < 0.01$), and the addition of PDA-NPS further enhanced such a positive effect. However, no statistical difference in this effect was observed between the CADMS-G-2-Hep-CGF group and the CADMS-G-4-Hep-CGF group (NS, $p > 0.05$).

Cell adhesion and proliferation experiments

L929 cells and HUVEC were inoculated for 3 days. As shown in Figure 8A, cells in each group grew well, distributed along the material's pores, and adhered to many living cells, with no statistical difference between groups (Figure 8D) (NS, $p > 0.05$). Co-culture of material extract and cells can reflect the cytotoxicity of the material to a certain extent.[45] The morphological results of cells in Figure 8B showed that heparinized CADMS-G did not affect cell morphology, and the addition of PDA-NPS promoted cell proliferation to a certain extent. No difference was observed between the CADMS-G-2-Hep-CGF group and the CADMS-G-4-Hep-CGF group. Fluorescence staining results (Figure 8C) of 4, 6-diamidino-2-phenylindole–photolipin showed that HUVEC were closely attached to the pore walls of each group of materials after 3 days of culture, and typical polygonal cells with normal morphology could be observed. Moreover, quantitative fluorescence results (Figure 8E) showed that HUVEC cultured in the CADMS-G-2-Hep-CGF group and CADMS-G-4-Hep-CGF group had the most potent proliferation ability ($p < 0.001$). There was no statistical difference between the CADMS-G-2-Hep-CGF group and the CADMS-G-4-Hep-CGF group (NS, $p > 0.05$). These results jointly supported that optimized CADMS-G-2-Hep combined with CGF could promote the adhesion and proliferation of skin and soft tissue healing–related cells (HUVEC and L929 cells) on the material.

Preparation of CGF and evaluation of *in vitro* biocompatibility

CGF fibrin gel is a three-dimensional network structure composed of fibrin of varying thicknesses. The embodiment of a significant number of white blood cells indicates a strong ability to regulate inflammation

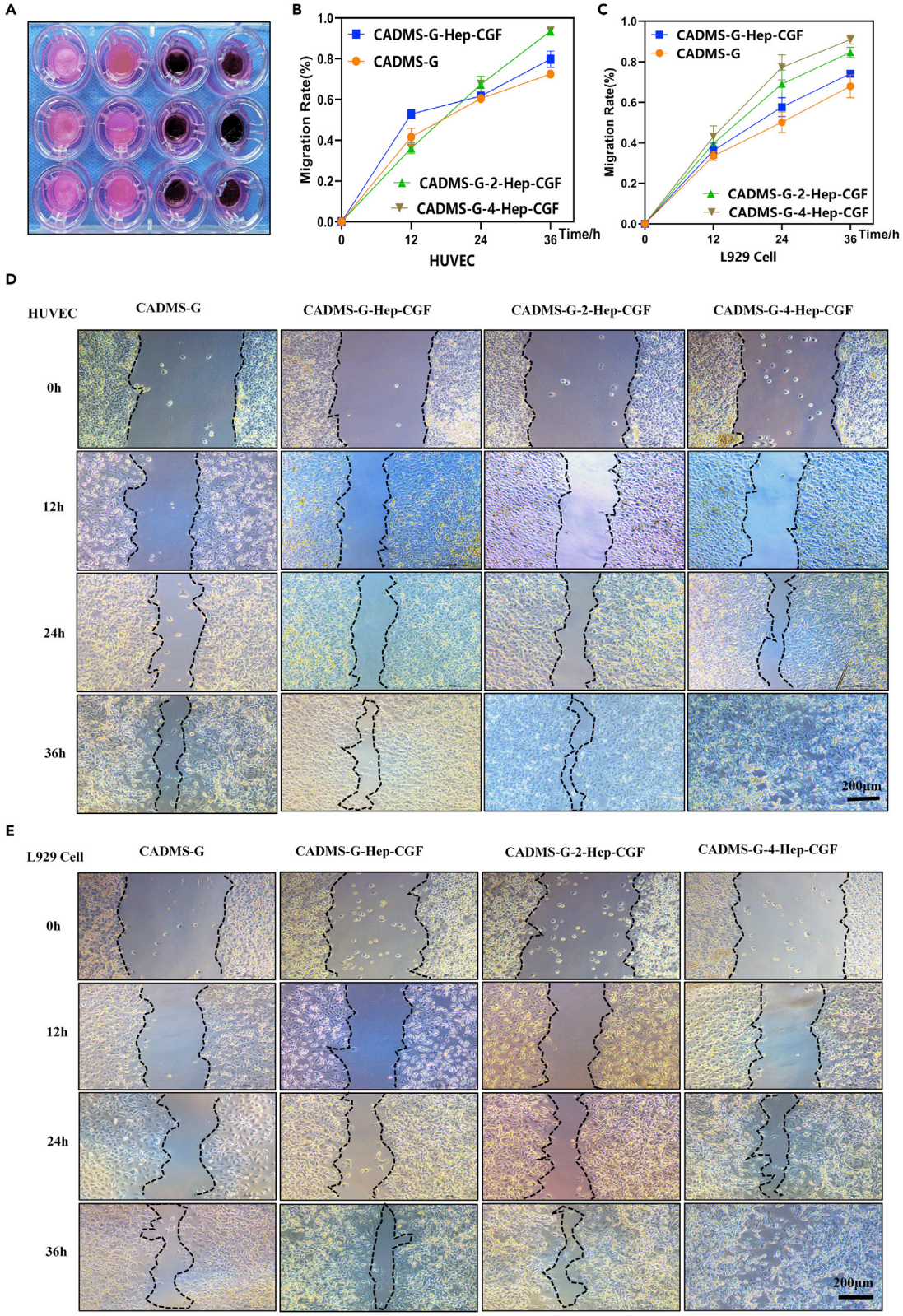
A
B
CADMS-G-Hep-CGF
CADMS-G
CADMS-G-2-Hep-CGF
CADMS-G-4-Hep-CGF
Migration Rate(%)
Time/h
HUVEC
C
L929 Cell
D
HUVEC
CADMS-G
CADMS-G-Hep-CGF
CADMS-G-2-Hep-CGF
CADMS-G-4-Hep-CGF
0h
12h
24h
36h
200μm
E
L929 Cell

Figure 7. The cell migration experiment evaluated the effect of multifunctional drug-delivered sponge scaffold materials on promoting cell migration

(A) Scratch experiment schematic diagram of the experimental process.
(B) Statistical quantification of HUVEC mobility.
(C) Statistical quantification of L929 cell mobility.
(D) Physical maps of HUVEC migration and change at different time points.
(E) Dynamic changes of L929 cell migration.

and fight infection.[4,5] Moreover, TGF-β, VEGF, and many CD34 (+) cells in the autologous CGF fibrin gel are essential for vascular maintenance, angiogenesis, and immune regulation.[46] As shown in Figure S2A, the CGF fibrin solution prepared by variable-speed centrifuge is also a light yellow liquid, which does not change significantly when standing at room temperature. After freeze-drying (Figure S2B), CGF with varying concentrations exhibited a loose, porous, and spongy structure with a brittle texture. When CGF with varying concentrations was incubated at 37°C for 24 h, the 10% and 15% CGF formed gel (Figure S2C). CCK-8 results (Figure S2D) showed that CGF concentrations less than 15% had no significant effect on cell proliferation, while CGF concentrations greater than 15% inhibited cell activity. In microscopic morphology (Figure S2E), CGF with varying concentrations had a particular three-dimensional fiber network structure and fragile texture.

L929 cells were cultured with varying concentrations of CGF (Figure S3A). The results showed that the CGF solution with a concentration below 20% could function as a 10% complete medium to maintain cell growth. However, CGF at concentrations greater than 20% could not support cell growth from 48 h. The cell migration experiment further optimized the concentration of CGF (Figure S3B) and found that 15% CGF achieved the best performance in promoting cell migration at 36 h. The 10% CGF continued to encourage cell migration for 48 h until the cells were in contact. Quantitative mobility results (Figure S3C) showed that 10% CGF achieved the best mobility at 48 h, followed by the control, and then the 15% CGF. In conclusion, the optimized 10% CGF has the best effect on cell proliferation and migration.

In vivo wound healing in the full-thickness skin defect model

To verify the effect of CADMS-G-2-Hep-CGF on *in vivo* wound healing, a full-thickness defect wound model of a rat's back was constructed, and CADMS-G-2-Hep-CGF combined with an autologous skin graft was used for wound repair.[47] The surgical design is shown in Figures 9A and 9B. On the seventh postoperative day, the grafts in the CADMS-G group showed signs of erosion, ischemia, and unshed scab while the grafts in the CADMS-G-2-Hep group showed slight necrosis, indicating that the grafts were unstable and immature. This verified that the artificial dermal stent needs a second transplant to establish blood supply.[9] The grafted skin of the CADMS-G-2-Hep-CGF group was flat and firmly attached to the recipient bed (Figure 9C). Nonviable skin grafts in each group tended to shrink over time (Figure 9G). On the seventh day, the residual unhealed skin graft areas of control, CADMS-G, CADMs-G-2-Hep, and CADMS-G-2-Hep-CGF were 9.64 $\pm$ 2.8 mm^2, 18.28 $\pm$ 2.16 mm^2, 11.57 $\pm$ 4.29 mm^2, and 6.05 $\pm$ 3.14 mm^2, respectively (Figure S4). The early survival rate of the CADMS-G-2-Hep-CGF group was significantly increased ($p < 0.01$). Similar conclusions were obtained from the observation of neovascularization on the skin[45]; that is, after loading CGF, the CADMS-G-2-Hep group showed more new vessels and muscular branches, and the regenerated microvessels could fuse with the existing vascular system (Figure 9D).

Histological analysis

H&E staining and Masson trichromatic staining

Hair follicles and their attached sebaceous glands are equivalent to the relevant components of reconstructed skin. H&E staining enabled us to analyze structural changes in the graft epidermis. As shown in Figure 9E, on day 14, the full-thickness skin grafts in each group mostly retained evenly distributed hair follicles. From day 14 to day 28, the follicles enlarged and grew hairs as the remodeling progressed. Survival after implantation depends primarily on adequate blood circulation, which provides nutrients essential for skin repair.[48] The development of functional neovascularization early in transplantation is associated with enhanced maintenance of healthy skin grafts, which prevents scar formation and subsequent contraction.[49] Figure 9F shows that the number of microvessels (characterized by endothelialized lumen containing red blood cells) in the CADMS-G-2-Hep-CGF group was significantly higher than that in the control group on days 14 and 28 after surgery (Figure 9H) ($p < 0.001$). Compared with intact skin,

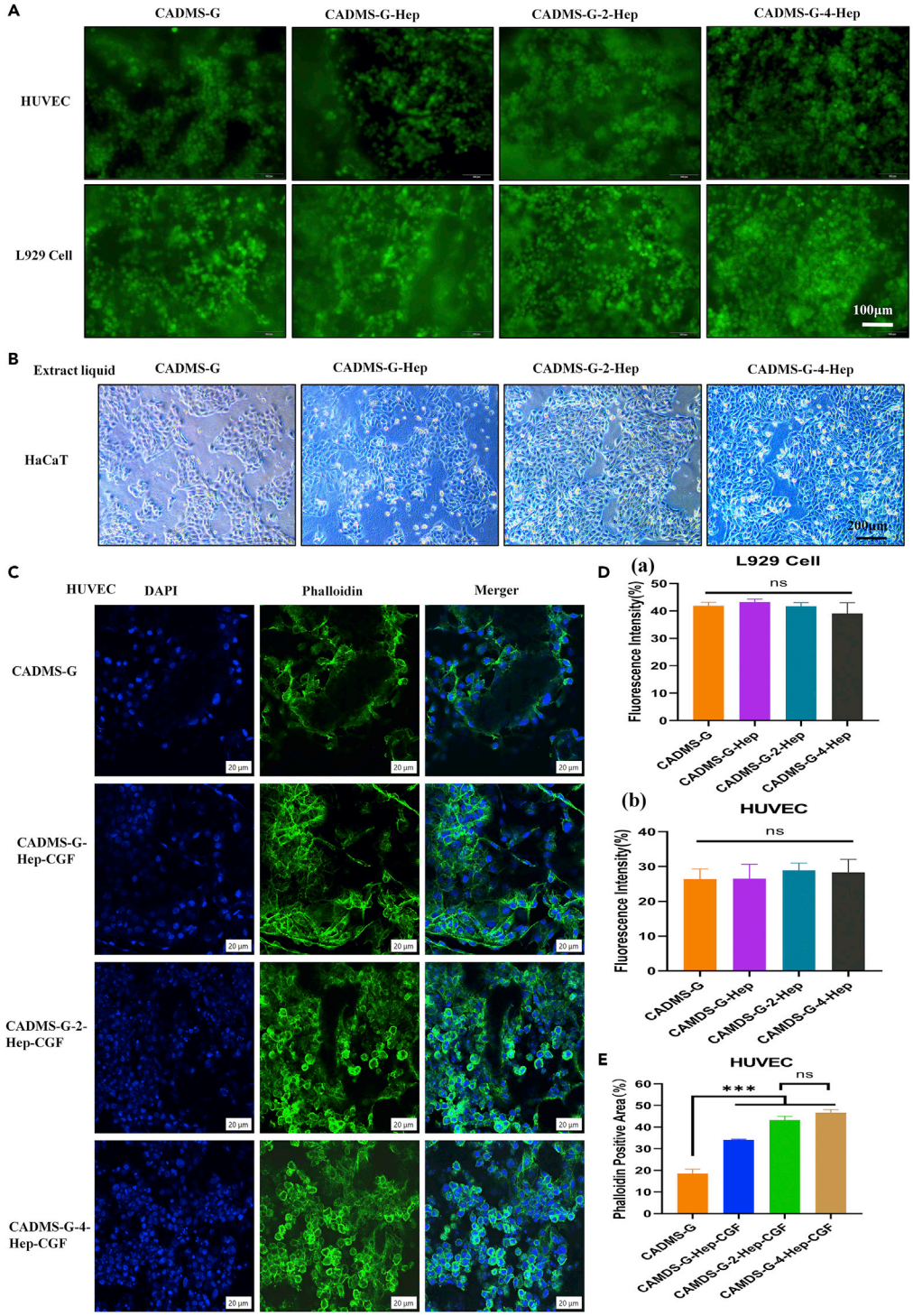

Figure 8. The biocompatibility of multifunctional sponge scaffold materials was evaluated at the *in vitro* cellular level

(A) Fluorescent staining of living and dead cells.

(B) Morphology of keratinocytes cultured with multifunctional sponge scaffold extract for 48 h.

(C) Fluorescence staining of DAPI-Photolipin.

(D) Statistical quantification of fluorescence intensity of living and dead cells.

(E) Statistical quantification of DAPI-positive fluorescence staining intensity (***$p < 0.001$).

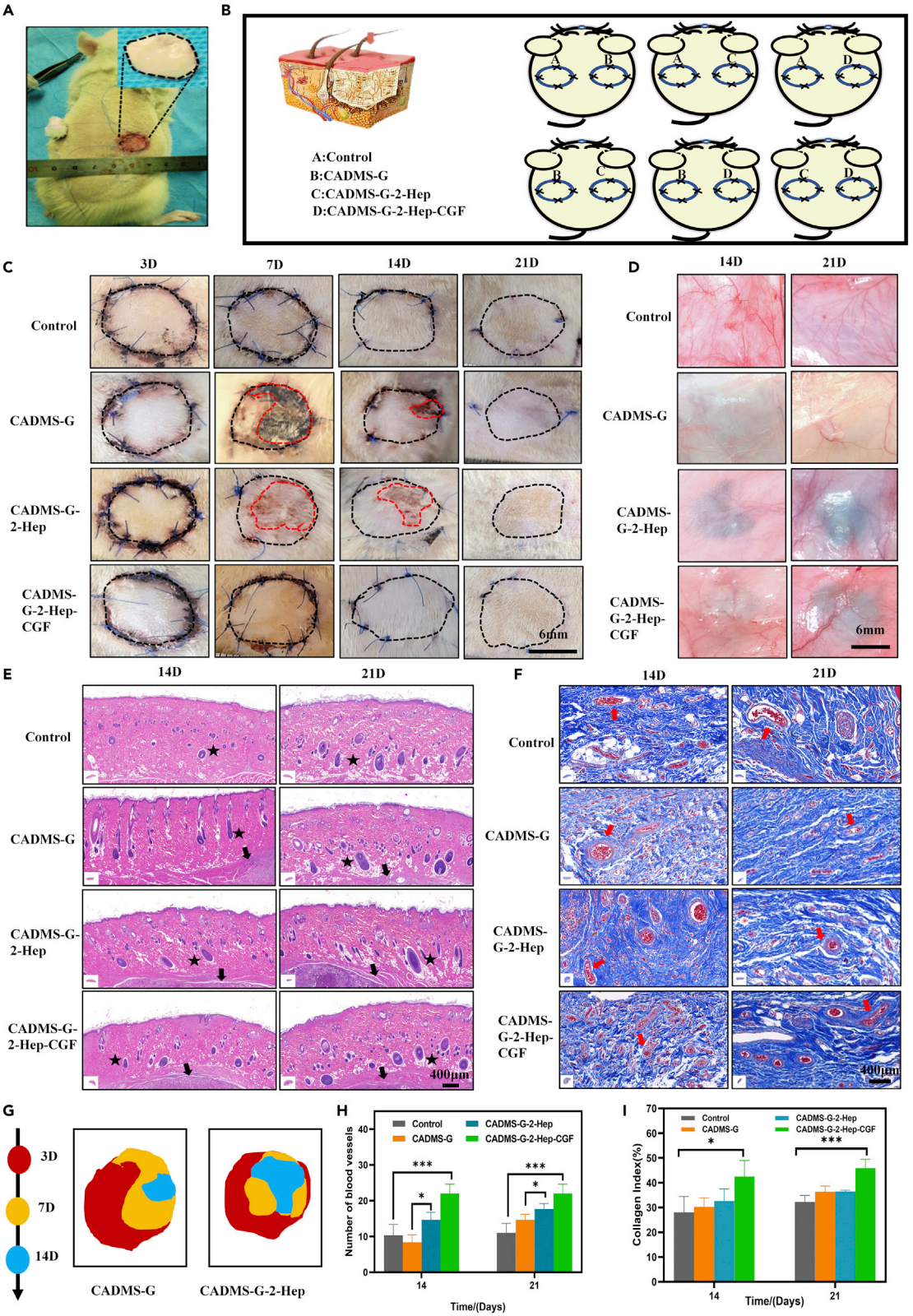
A
B
A:Control
B:CADMS-G
C:CADMS-G-2-Hep
D:CADMS-G-2-Hep-CGF
C
3D
7D
14D
21D
Control
CADMS-G
CADMS-G-2-Hep
CADMS-G-2-Hep-CGF
6mm
D
14D
21D
Control
CADMS-G
CADMS-G-2-Hep
CADMS-G-2-Hep-CGF
6mm
E
14D
21D
Control
CADMS-G
CADMS-G-2-Hep
CADMS-G-2-Hep-CGF
400μm
F
14D
21D
Control
CADMS-G
CADMS-G-2-Hep
CADMS-G-2-Hep-CGF
400μm
G
3D
7D
14D
CADMS-G
CADMS-G-2-Hep
H
Control
CADMS-G
CADMS-G-2-Hep
CADMS-G-2-Hep-CGF
Number of blood vessels
Time/(Days)
I
Control
CADMS-G
CADMS-G-2-Hep
CADMS-G-2-Hep-CGF
Collagen Index(%)
Time/(Days)

Figure 9. Evaluation of wound healing

(A) Schematic diagram of the application of different scaffolds in rat wounds.

(B) Schematic diagram of autologous skin transplantation combined with drug-loaded scaffold transplantation in rats.

(C) Representative images of survival at each time point after full-thickness skin graft injury. The edges of the unhealed wound are encircled by a red dotted line.

(D) Overview of neovascularization on days 14 and 21 after different treatments.

(E) H&E staining of graft sections collected at different time points from varying hair follicles (black star) and implants (black arrow).

(F) Masson's trichromatic staining of skin grafts and blood vessels (red arrow).

(G) Changes of unhealed wounds on days 3, 7, and 14 after injury.

(H) Quantitative vascular analysis.

(I) Quantitative analysis of collagen staining strength in histological sections (*$p < 0.05$, ***$p < 0.001$).

collagen fibers in scar tissue are more densely arranged and linear in the direction of tension, leading to myofibroblast proliferation and scar contraction.[50] Collagen deposition and tissue in skin grafts were analyzed by Masson trichromatic staining (blue areas represent collagen). As shown in Figure 9F, on the 14th day after surgery, collagen fibers in the CADMS-G group and the CADMS-G-2-Hep group were arranged compactly while the skin grafts in the CADMS-G-2-Hep-CGF group and the control group had loose collagen fibers, which reduced scar formation. The quantitative image analysis results further supported these observations (Figure 9I). On the 14th day after surgery, collagen deposition in the CADMS-G-2-Hep-CGF group was higher than that in the control group ($p < 0.05$). As time went by, on day 28, compared with the control group, more orderly collagens were observed in the CADMS-G-2-Hep-CGF group, which facilitated the migration and infiltration of fibroblasts to the wound surface, thus stimulating the secretion of more mature collagens. However, disordered and immature collagens in the CADMS-G group may contribute to scar hyperplasia.[45]

Immunofluorescence staining

Ki67 is an antigen associated with proliferation cells, whose function is closely related to mitosis and is indispensable for cell proliferation.[51] Ki67 expression was significantly increased in skin grafts and hair follicles in the CADMS-G-2-Hep-CGF group (Figures 10A and 10B). Fluorescence quantitative results showed the same trend (Figures 10C and 10D), with significant statistical differences. These results indicated that adding CGF promotes the proliferation and migration of graft skin cells, enabling the wounded area to develop from a repair stage characterized by re-epithelialization and granulation tissue development to a functional remodeling stage.[5,45]

NIR photothermal conversion promotes the healing of wound grafts

In vivo, full-thickness skin defect repair experiments showed that the incorporation of CGF promoted wound healing. The NIR light and heat conversion can boost the recovery of the wound graft. The surgical design scheme is shown in Figures 11A and 11B. The results showed that the wound temperature in the CADMS-G-2-Hep group reached 44 $\pm$ 0.8°C after 30 min of NIR light irradiation, compared with 38.2 $\pm$ 0.7°C in the control group. Besides, the grafts in each group began to heal without any infection after surgery (Figure 11C). As shown in Figure 11F and 11G, the CADMS-G-2-Hep-CGF-INR group had a lower skin shrinkage rate than the CADMS-G-2-Hep group and the CADMS-G-2-Hep-INR group. The CADMS-G-2-Hep-CGF group had a lower skin shrinkage rate than the CADMS-G-2-Hep group. The above results showed that adding CGF contributed to skin survival, and the incorporation of INR further amplified this effect. We speculated that mild local heating (41°C–43°C) could induce the proliferation of vascular endothelial cells and effectively increase the vascular density in the new granulation tissue, thus improving the survival of autologous skin grafts.[41]

H&E staining

Locally administered scaffold materials can accumulate in various organs through the blood circulation system, which may cause early and late toxicity of organs.[52] From each experimental animal, the heart, liver, spleen, lungs, and kidneys were collected and stained with H&E on days 3 and 21 (Figure 11D). The histomorphology results showed no noticeable pathological changes in all organs, such as cell necrosis, swelling, and congestion, and only slight inflammatory cell infiltration in the liver was observed. Yet, no significant differences were observed in other organs. H&E staining results (Figure 11E) showed that compared with the CADMS-G-2-Hep group, the CADMS-G-2-Hep-CGF group was beneficial to the regeneration of graft skin appendage, and new tissue in this group infiltrated into the porous structure of the composite scaffold. For the CADMS-G-2-Hep-CGF group irradiated by NIR light, the regeneration rate

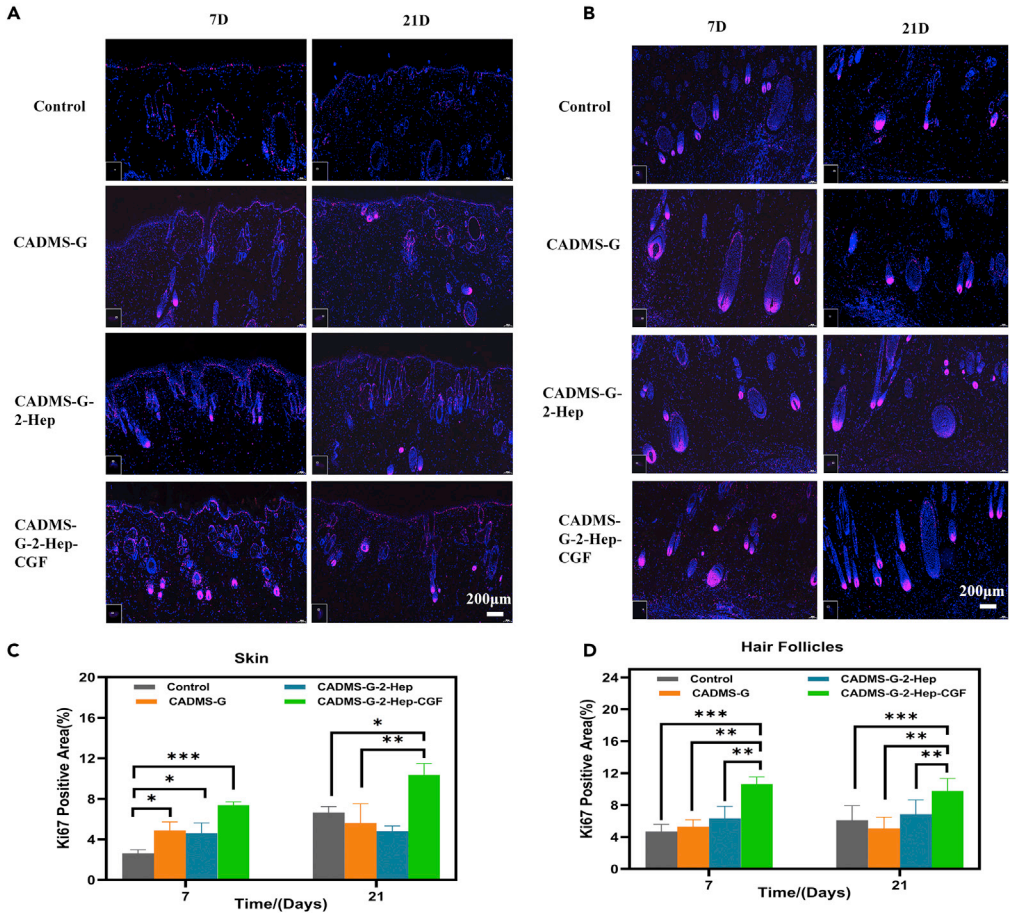

Figure 10. Immunofluorescence staining images of Ki67 in skin tissues of rats treated in different drug administration groups

(A) Full skin.

(B) Hair follicles.

(C) Full-thickness skin fluorescence quantification.

(D) Immunofluorescence quantification of hair follicles (*$p < 0.05$, **$p < 0.01$, ***$p < 0.001$).

of the skin graft accessory was further increased, and the regenerated tissue was more mature, similar to natural hair follicle tissue. These results indicated that the composite scaffold incorporated with PDA-NPS could respond to NIR stimulation and perform NIR photothermal therapy to promote skin tissue regeneration.[40,41] Moreover, the incorporation of CGF was in synergy with NIR photothermal therapy to speed up wound healing.

Immunohistochemical staining

The wound repair process is often accompanied by wound contraction and scar formation. As the material basis of scar contraction, Alpha smooth muscle actin (α-SMA) determines the outcome of a scar.[53] Figures 12A and 12C show that the distribution of α-SMA in the CADMS-G-2-Hep-CGF-INR group was less than that in the other three groups, followed by the CADMS-G-2-Hep-INR group, CADMS-G-2-Hep-CGF group, and CADMS-G-2-Hep group. There was statistical significance ($p < 0.05$). These results indicated that the CADMS-G-2-Hep-CGF-INR group inhibited α-SMA deposition and ultimately reduced scar formation. Neovascularization provides oxygen and nutrients for wound repair and affects cell tissue proliferation and remodeling. Therefore, CD31 was used to label vascular endothelial cells to analyze the degree of vascular formation during wound healing.[54] Figures 12B and 12D showed a more extensive distribution of CD31 (+) cells and blood vessels with a larger diameter in the CADMS-G-2-Hep-INR group than in the other three groups, indicating that CADMS-G-2-Hep-INR could accelerate the formation of blood vessels in the wound-healing process.

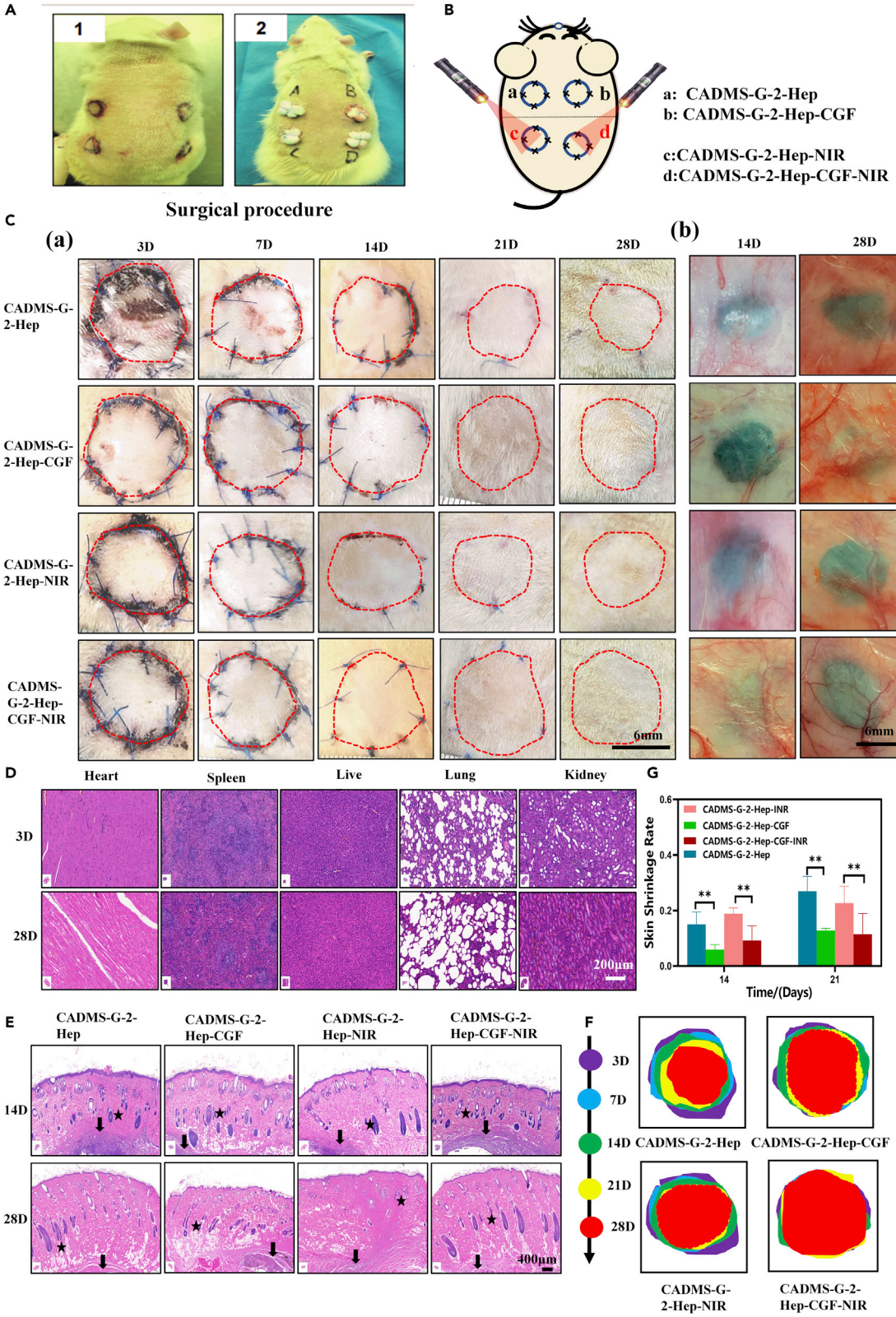
A
1
2
Surgical procedure
B
a
b
c
d
a: CADMS-G-2-Hep
b: CADMS-G-2-Hep-CGF
c:CADMS-G-2-Hep-NIR
d:CADMS-G-2-Hep-CGF-NIR
C
(a)
3D
7D
14D
21D
28D
(b)
14D
28D
CADMS-G-2-Hep
CADMS-G-2-Hep-CGF
CADMS-G-2-Hep-NIR
CADMS-G-2-Hep-CGF-NIR
6mm
6mm
D
Heart
Spleen
Live
Lung
Kidney
3D
28D
200μm
G
CADMS-G-2-Hep-INR
CADMS-G-2-Hep-CGF
CADMS-G-2-Hep-CGF-INR
CADMS-G-2-Hep
Skin Shrinkage Rate
0.6
0.4
0.2
0.0
14
21
Time/(Days)
**
E
CADMS-G-2-Hep
CADMS-G-2-Hep-CGF
CADMS-G-2-Hep-NIR
CADMS-G-2-Hep-CGF-NIR
14D
28D
400μm
F
3D
7D
14D
21D
28D
CADMS-G-2-Hep
CADMS-G-2-Hep-CGF
CADMS-G-2-Hep-NIR
CADMS-G-2-Hep-CGF-NIR

Figure 11. Evaluation of wound healing under NIR photothermal therapy

(A) Images of applying different scaffolds in rat wounds.

(B) Schematic diagram of autologous skin transplantation in rats under NIR photothermal treatment.

(C) Representative images of survival at each time point after full-thickness skin graft injury: A. The edge of the graft is encircled by a red dotted line; B. vascularization images of implanted stent materials.

(D) H&E staining results of rat viscera.

(E) H&E staining of graft sections collected at different time points from varying hair follicles (black star) and implants (black arrow).

(F) Shrinkage of grafted skin on days 3, 7, 14, 21, and 28 after injury (**p < 0.01).

(G) Quantitative analysis of skin shrinkage rate (*P<0.05, **P<0.01, ***P<0.001).

In general, it is reasonable to infer that the positive effect of the CADMS-G-2-Hep-INR group on wound repair may come from the following aspects: First, the CADMS-G-2-Hep composite scaffold can provide a 3D microporous structure similar to extracellular matrix, which can promote cell adhesion and proliferation and induce tissue growth[55]; second, CADMS-G-2-Hep composite scaffolds have good liquid absorption capacity and can absorb nutrients and components around host tissues to promote cell growth and regeneration[56]; third, heparin-modified sponge scaffolds improved the loading capacity and controlled the release effect of GFs, which enabled them to maintain local CGF concentrations at high levels, thus boosting angiogenesis and tissue repair more effectively[57]; and finally, CADMS-G-2-Hep has an excellent photothermal conversion performance and can respond to external NIR stimulation to accelerate blood flow, improve substance metabolism, and promote tissue regeneration.[58]

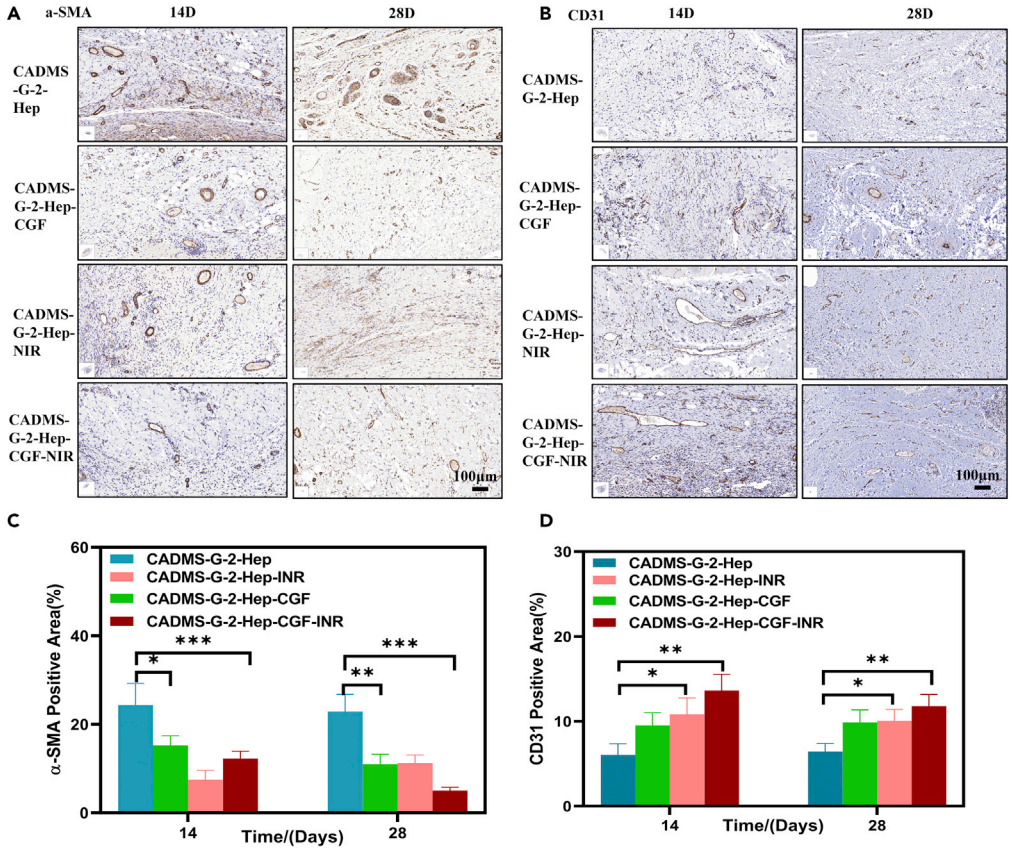

Figure 12. Immunohistochemical analysis of different groups on day 14 and day 28

(A) Immunohistochemical staining images of CD31 in each group.

(B) Immunohistochemical images of α-SMA in each group.

(C) Quantitative analysis of α-SMA.

(D) Quantitative analysis of CD31 (*p < 0.05, **p < 0.01, ***p < 0.001).

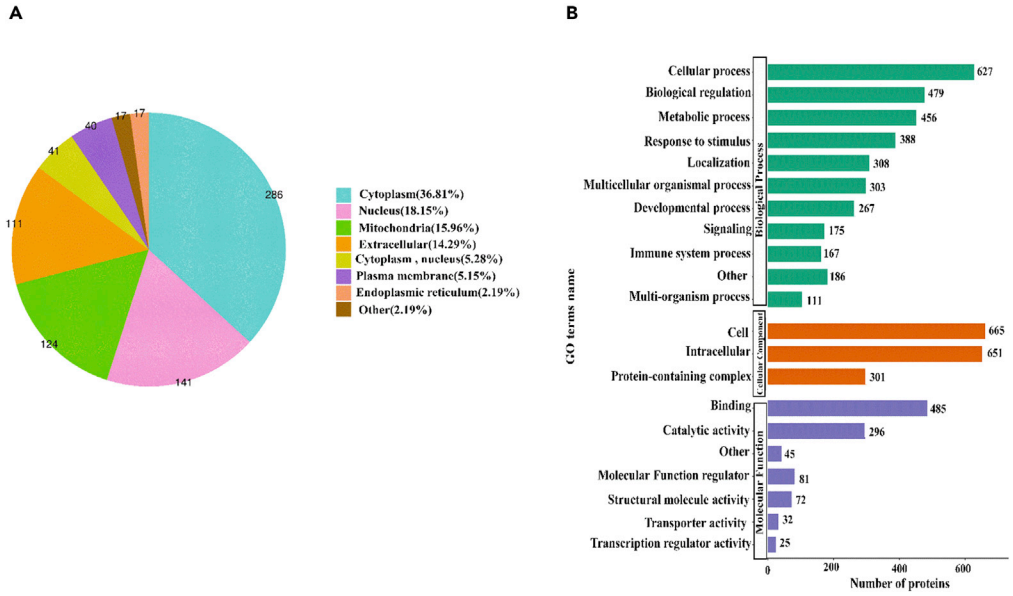

Figure 13. Quantitative protein analysis in white Tibet miniature pig skin and porcine ADM sponge based on mass spectrometry

(A) Subcellular distribution of differentially expressed proteins.

(B) Biological processes and molecular function categories of differentially expressed proteins.

Analysis of differences in proteomic characteristics and functional categories of identified proteins in pig skin

Quantitative analysis results of Tibetan miniature pig skin and the porcine decellularized dermal matrix protein sponge showed that a total of 777 differentially expressed proteins were detected before and after decellularization, which were mainly from the cytoplasm, the nucleus, and the extracellular space and plasma membrane (Figure 13A). This means those removed by decellularization were mainly the components of the nucleus and cytoplasm, and most extracellular matrix components were retained.[59] Gene ontology (GO) analysis of biological processes showed that the porcine ADM was mainly involved in cellular processes, natural regulation, and metabolic processes, and its three most abundant molecular functions are binding, catalytic activity, and functional molecular regulators (Figure 13B). This provides a basis for further research on the possible molecular mechanism of PADMS promoting wound healing.

DISCUSSION

In summary, we have successfully prepared a novel multifunctional composite repair scaffold (CADMS-G-2-Hep) that has good biocompatibility and tissue affinity and can effectively promote skin regeneration and wound healing in response to external NIR stimulation. The composite can effectively adhere to more CGF and achieve a more durable release of GFs. In *in vitro* cell experiments and *in vivo* animal experiments, this complex biomaterial was able to maintain the biological activity of CGF; promote angiogenesis, cell proliferation, and tissue adhesion; improve the skin sheet survival of full-thickness skin defect wounds while reducing graft contraction and scar formation; and boost wound healing and tissue reconstruction. It provides a new idea for the design and development of artificial dermis in the field of biological tissue engineering.

Limitations of the study

There are still some limitations to this study. In this study, by the time the *in vivo* degradation experiment ended at 16 weeks, the scaffold material had not entirely degraded. The *in vivo* degradation products have not been identified, which will be improved in our future study. Besides, given that there were four different wounds on each rat's back, we could not compare the difference in GF's release *in vivo* and its effect on body circulation by an analysis of the collected whole blood of rats. Considering the significant differences in the structure and function between SD rat skin and human skin, whether the effect of autologous skin transplantation can fully reflect the healing effect of human skin transplantation needs further research to confirm.

STAR★METHODS

Detailed methods are provided in the online version of this paper and include the following:

- KEY RESOURCES TABLE
- RESOURCE AVAILABILITY
  - Lead contact
  - Materials availability
  - Data and code availability
- EXPERIMENTAL MODEL AND SUBJECT DETAILS
  - Cell lines
- METHOD DETAILS
  - Preparation of an acellular dermal matrix-chitosan composite sponge scaffold
  - Preparation of heparin sodium modified composite sponge scaffold
  - Preparation of composite sponge scaffolds doped with polydopamine nanosphere
  - Preparation of concentrated growth factor delivery sustained-release scaffold
  - Physical and chemical properties characterization of materials
  - Cytotoxicity test
  - Scratch test
  - Staining of living and dead cells
  - Cell proliferation and adhesion experiments
  - *In vivo* wound healing in a full-layer skin model
  - Skin graft survival, contraction, and capillary density
  - H&E and Masson trichromatic staining
  - Immunohistochemical staining of Ki67, CD31, and α-SMA
  - Proteomic analysis
  - Statistical analysis

SUPPLEMENTAL INFORMATION

Supplemental information can be found online at https://doi.org/10.1016/j.isci.2022.105835.

ACKNOWLEDGMENTS

This work was supported by the Natural Science Foundation of Guangdong Province (no. 2020 A151501108), the Guangdong Province Key Field R&D Program Project (no. 2020B1111150001), the Science and Technology Innovation Project of Guangdong Province (no. 2018KJYZ005), and the Natural Science Foundation of Tibet Autonomous Region (no. XZ2017ZR-ZY021).

AUTHOR CONTRIBUTIONS

Investigation, methodology, experimental data acquisition, supervision, writing–first draft: L.L.C.; investigation, methodology, experimental data acquisition: C.Y.H., Y.Z., and Y.J.C.; investigation, experimental data acquisition, validation: H.H.Z. and Z.W.J.; investigation, supervision, validation: Z.J.Z., C.Y.H., and L.H.; investigation, visualization: X.R.W., Y.J.P., and L.B.N.; funding acquisition, supervision, writing–first draft, writing–review and editing: Y.B.G., J.M., and L.Y. All authors have read and agreed to the published version of the article.

DECLARATION OF INTERESTS

The authors declare no competing interests.

The animal use procedures for the rat full-thickness defect wound experiment were approved by the international animal care and use committee (NFYY-2022-0105).

Received: October 11, 2022
Revised: November 10, 2022
Accepted: December 16, 2022
Published: January 20, 2023

REFERENCES

1. Nourian Dehkordi, A., Mirahmadi Babaheydari, F., Chehelgerdi, M., and Raeisi Dehkordi, S. (2019). Skin tissue engineering: wound healing based on stem-cell-based therapeutic strategies. Stem Cell Res. Ther. *10*, 111. https://doi.org/10.1186/s13287-019-1212-2.

2. Meuli, M., Hartmann-Fritsch, F., Hüging, M., Marino, D., Saglini, M., Hynes, S., Neuhaus, K., Manuel, E., Middelkoop, E., Reichmann, E., and Schiestl, C. (2019). A cultured autologous dermo-epidermal skin substitute for full-thickness skin defects: a phase I, open, prospective clinical trial in children. Plast. Reconstr. Surg. *144*, 188–198. https://doi.org/10.1097/PRS.0000000000005746.

3. Grishkevich, V.M. (2009). The post-burn elbow medial flexion scar contracture treatment with trapeze-flap plasty. Burns *35*, 280–287. https://doi.org/10.1016/j.burns.2008.06.001.

4. Li, Z., Liu, L., Wang, L., and Song, D. (2021). The effects and potential applications of concentrated growth factor in dentin-pulp complex regeneration. Stem Cell Res. Ther. *12*, 357. https://doi.org/10.1186/s13287-021-02446-y.

5. Tabatabaei, F., Aghamohammadi, Z., and Tayebi, L. (2020). In vitro and in vivo effects of concentrated growth factor on cells and tissues. J. Biomed. Mater. Res. *108*, 1338–1350. https://doi.org/10.1002/jbm.a.36906.

6. Everts, P., Onishi, K., Jayaram, P., Lana, J.F., and Mautner, K. (2020). Platelet-rich plasma: new performance understandings and therapeutic considerations in 2020. Int. J. Mol. Sci. *21*, 7794. https://doi.org/10.3390/ijms21207794.

7. Chopra, H., Kumar, S., and Singh, I. (2021). Biopolymer-based scaffolds for tissue engineering applications. Curr. Drug Targets *22*, 282–295. https://doi.org/10.2174/1389450121999201102140408.

8. Dai, C., Shih, S., and Khachemoune, A. (2020). Skin substitutes for acute and chronic wound healing: an updated review. J. Dermatolog. Treat. *31*, 639–648. https://doi.org/10.1080/09546634.2018.1530443.

9. Qiu, X., Wang, J., Wang, G., and Wen, H. (2018). Vascularization of Lando® dermal scaffold in an acute full-thickness skin-defect porcine model. J. Plast. Surg. Hand Surg. *52*, 204–209. https://doi.org/10.1080/2000656X.2017.1421547.

10. Li, M., Ma, J., Gao, Y., Dong, M., Zheng, Z., Li, Y., Tan, R., She, Z., and Yang, L. (2020). Epithelial differentiation of human adipose-derived stem cells (hASCs) undergoing three-dimensional (3D) cultivation with collagen sponge scaffold (CSS) via an indirect co-culture strategy. Stem Cell Res. Ther. *11*, 141. https://doi.org/10.1186/s13287-020-01645-3.

11. Przekora, A. (2020). A concise review on tissue engineered artificial skin grafts for chronic wound treatment: can we reconstruct functional skin tissue in vitro? Cells *9*, 1622. https://doi.org/10.3390/cells9071622.

12. Reid, M.J., Currie, L.J., James, S.E., and Sharpe, J.R. (2007). Effect of artificial dermal substitute, cultured keratinocytes and split thickness skin graft on wound contraction. Wound Repair Regen. *15*, 889–896. https://doi.org/10.1111/j.1524-475X.2007.00313.x.

13. Haney, N.M., Huang, M.M., Liu, J.L., Hawksworth, D.J., and Burnett, A.L. (2021). Acellular dermal matrix tissues in genitourinary reconstructive surgery: a review of the literature and case discussions. Sex. Med. Rev. *9*, 488–497. https://doi.org/10.1016/j.sxmr.2020.07.003.

14. Kirsner, R.S., Bohn, G., Driver, V.R., Mills, J.L., Nanney, L.B., Williams, M.L., and Wu, S.C. (2015). Human acellular dermal wound matrix: evidence and experience. Int. Wound J. *12*, 646–654. https://doi.org/10.1111/iwj.12185.

15. Shang, F., and Hou, Q. (2021). Effects of allogenic acellular dermal matrix combined with autologous razor-thin graft on hand appearance and function of patients with extensive burn combined with deep hand burn. Int. Wound J. *18*, 279–286. https://doi.org/10.1111/iwj.13532.

16. Lu, J., Cai, L., Dai, Y., Liu, Y., Zuo, F., Ni, C., Shi, M., and Li, J. (2021). Polydopamine-based nanoparticles for photothermal therapy/chemotherapy and their synergistic therapy with autophagy inhibitor to promote antitumor treatment. Chem. Rec. *21*, 781–796. https://doi.org/10.1002/tcr.202000170.

17. Zheng, P., Ding, B., and Li, G. (2020). Polydopamine-incorporated nanoformulations for biomedical applications. Macromol. Biosci. *20*, e2000228. https://doi.org/10.1002/mabi.202000228.

18. Zhang, P., Li, X., Xu, Q., Wang, Y., and Ji, J. (2021). Polydopamine nanoparticles with different sizes for NIR-promoted gene delivery and synergistic photothermal therapy. Colloids Surf. B Biointerfaces *208*, 112125. https://doi.org/10.1016/j.colsurfb.2021.112125.

19. Davidenko, N., Gibb, T., Schuster, C., Best, S.M., Campbell, J.J., Watson, C.J., and Cameron, R.E. (2012). Biomimetic collagen scaffolds with anisotropic pore architecture. Acta Biomater. *8*, 667–676. https://doi.org/10.1016/j.actbio.2011.09.033.

20. Chen, L., Ma, J., Chen, Y., Huang, C., Zheng, Z., Gao, Y., Jiang, Z., Wei, X., Peng, Y., Yu, S., and Yang, L. (2022). Polydopamine modified acellular dermal matrix sponge scaffold loaded with a-FGF: promoting wound healing of autologous skin grafts. Biomater. Adv. *136*, 212790. https://doi.org/10.1016/j.bioadv.2022.212790.

21. Ratanavaraporn, J., Kanokpanont, S., Tabata, Y., and Damrongsakkul, S. (2008). Effects of acid type on physical and biological properties of collagen scaffolds. J. Biomater. Sci. Polym. Ed. *19*, 945–952. https://doi.org/10.1163/156856208784613505.

22. Yang, H., Duan, L., Li, Q., Tian, Z., and Li, G. (2018). Experimental and modeling investigation on the rheological behavior of collagen solution as a function of acetic acid concentration. J. Mech. Behav. Biomed. Mater. *77*, 125–134. https://doi.org/10.1016/j.jmbbm.2017.09.003.

23. Perez-Puyana, V., Jiménez-Rosado, M., Romero, A., and Guerrero, A. (2019). Crosslinking of hybrid scaffolds produced from collagen and chitosan. Int. J. Biol. Macromol. *139*, 262–269. https://doi.org/10.1016/j.ijbiomac.2019.07.198.

24. Davoudi, Z., Peroutka-Bigus, N., Bellaire, B., Jergens, A., Wannemuehler, M., and Wang, Q. (2021). Gut organoid as a new platform to study alginate and chitosan mediated PLGA nanoparticles for drug delivery. Mar. Drugs *19*, 282. https://doi.org/10.3390/md19050282.

25. Hu, W., Liu, M., Yang, X., Zhang, C., Zhou, H., Xie, W., Fan, L., and Nie, M. (2019). Modification of chitosan grafted with collagen peptide by enzyme crosslinking. Carbohydr. Polym. *206*, 468–475. https://doi.org/10.1016/j.carbpol.2018.09.023.

26. Tian, Z., Wu, K., Liu, W., Shen, L., and Li, G. (2015). Two-dimensional infrared spectroscopic study on the thermally induced structural changes of glutaraldehyde-crosslinked collagen. Spectrochim. Acta Mol. Biomol. Spectrosc. *140*, 356–363. https://doi.org/10.1016/j.saa.2015.01.003.

27. Peng, J., Zhao, H., Tu, C., Xu, Z., Ye, L., Zhao, L., Gu, Z., Zhao, D., Zhang, J., and Feng, Z. (2020). In situ hydrogel dressing loaded with heparin and basic fibroblast growth factor for accelerating wound healing in rat. Mater. Sci. Eng. C Mater. Biol. Appl. *116*, 111169. https://doi.org/10.1016/j.msec.2020.111169.

28. Mulloy, B., Hogwood, J., Gray, E., Lever, R., and Page, C.P. (2016). Pharmacology of heparin and related drugs. Pharmacol. Rev. *68*, 76–141. https://doi.org/10.1124/pr.115.011247.

29. Chen, J., Zhan, Y., Wang, Y., Han, D., Tao, B., Luo, Z., Ma, S., Wang, Q., Li, X., Fan, L., et al. (2018). Chitosan/silk fibroin modified nanofibrous patches with mesenchymal stem cells prevent heart remodeling post-myocardial infarction in rats. Acta Biomater. *80*, 154–168. https://doi.org/10.1016/j.actbio.2018.09.013.

30. Adamiak, K., and Sionkowska, A. (2020). Current methods of collagen cross-linking: Review. Int. J. Biol. Macromol. *161*, 550–560. https://doi.org/10.1016/j.ijbiomac.2020.06.075.

31. Rezaii, M., Oryan, S., and Javeri, A. (2019). Curcumin nanoparticles incorporated collagen-chitosan scaffold promotes cutaneous wound healing through regulation of TGF-β1/Smad7 gene expression. Mater. Sci. Eng. C Mater. Biol. Appl. *98*, 347–357. https://doi.org/10.1016/j.msec.2018.12.143.

32. Ma, L., Gao, C., Mao, Z., Zhou, J., Shen, J., Hu, X., and Han, C. (2003). Collagen/chitosan porous scaffolds with improved biostability for skin tissue engineering. Biomaterials *24*,

4833–4841. https://doi.org/10.1016/s0142-9612(03)00374-0.

33. Ishihara, J., Ishihara, A., Starke, R.D., Peghaire, C.R., Smith, K.E., McKinnon, T.A.J., Tabata, Y., Sasaki, K., White, M.J.V., Fukunaga, K., et al. (2019). The heparin binding domain of von Willebrand factor binds to growth factors and promotes angiogenesis in wound healing. Blood *133*, 2559–2569. https://doi.org/10.1182/blood.2019000510.

34. Tardalkar, K., Marsale, T., Bhamare, N., Kshersagar, J., Chaudhari, L., and Joshi, M.G. (2022). Heparin immobilization of tissue engineered xenogeneic small diameter arterial scaffold improve endothelialization. Tissue Eng. Regen. Med. *19*, 505–523. https://doi.org/10.1007/s13770-021-00411-7.

35. Tang, Y., Tan, Y., Lin, K., and Zhu, M. (2021). Research progress on polydopamine nanoparticles for tissue engineering. Front. Chem. *9*, 727123. https://doi.org/10.3389/fchem.2021.727123.

36. Lin, K., Gan, Y., Zhu, P., Li, S., Lin, C., Yu, S., Zhao, S., Shi, J., Li, R., and Yuan, J. (2021). Hollow mesoporous polydopamine nanospheres: synthesis, biocompatibility and drug delivery. Nanotechnology *32*, 285602. https://doi.org/10.1088/1361-6528/abf4a9.

37. Harris, Y., Sason, H., Niezni, D., and Shamay, Y. (2022). Automated discovery of nanomaterials via drug aggregation induced emission. Biomaterials *289*, 121800. https://doi.org/10.1016/j.biomaterials.2022.121800.

38. Rashki, S., Asgarpour, K., Tarrahimofrad, H., Hashemipour, M., Ebrahimi, M.S., Fathizadeh, H., Khorshidi, A., Khan, H., Marzhoseyni, Z., Salavati-Niasari, M., and Mirzaei, H. (2021). Chitosan-based nanoparticles against bacterial infections. Carbohydr. Polym. *251*, 117108. https://doi.org/10.1016/j.carbpol.2020.117108.

39. Guo, Z., Zhang, Z., Zhang, N., Gao, W., Li, J., Pu, Y., He, B., and Xie, J. (2022). A Mg2+/polydopamine composite hydrogel for the acceleration of infected wound healing. Bioact. Mater. *15*, 203–213. https://doi.org/10.1016/j.bioactmat.2021.11.036.

40. Sun, Y., and Davis, E.W. (2019). Facile fabrication of polydopamine nanotubes for combined chemo-photothermal therapy. J. Mater. Chem. B *7*, 6828–6839. https://doi.org/10.1039/c9tb01338e.

41. Maleki, A., He, J., Bochani, S., Nosrati, V., Shahbazi, M.A., and Guo, B. (2021). Multifunctional photoactive hydrogels for wound healing acceleration. ACS Nano *15*, 18895–18930. https://doi.org/10.1021/acsnano.1c08334.

42. Zheng, M., Wang, X., Chen, Y., Yue, O., Bai, Z., Cui, B., Jiang, H., and Liu, X. (2022). A review of recent progress on collagen-based biomaterials. Adv. Healthc. Mater. e2202042. https://doi.org/10.1002/adhm.202202042.

43. Cao, Y., Shi, X., Zhao, X., Chen, B., Li, X., Li, Y., Chen, Y., Chen, C., Lu, H., and Liu, J. (2022). Acellular dermal matrix decorated with collagen-affinity peptide accelerate diabetic wound healing through sustained releasing Histatin-1 mediated promotion of angiogenesis. Int. J. Pharm. *624*, 122017. https://doi.org/10.1016/j.ijpharm.2022.122017.

44. Wu, J., Zhu, J., He, C., Xiao, Z., Ye, J., Li, Y., Chen, A., Zhang, H., Li, X., Lin, L., et al. (2016). Comparative study of heparin-poloxamer hydrogel modified bFGF and aFGF for in vivo wound healing efficiency. ACS Appl. Mater. Interfaces *8*, 18710–18721. https://doi.org/10.1021/acsami.6b06047.

45. Zheng, Z., Li, M., Shi, P., Gao, Y., Ma, J., Li, Y., Huang, L., Yang, Z., and Yang, L. (2021). Polydopamine-modified collagen sponge scaffold as a novel dermal regeneration template with sustained release of platelet-rich plasma to accelerate skin repair: a one-step strategy. Bioact. Mater. *6*, 2613–2628. https://doi.org/10.1016/j.bioactmat.2021.01.037.

46. Rodella, L.F., Favero, G., Boninsegna, R., Buffoli, B., Labanca, M., Scarì, G., Sacco, L., Batani, T., and Rezzani, R. (2011). Growth factors, CD34 positive cells, and fibrin network analysis in concentrated growth factors fraction. Microsc. Res. Tech. *74*, 772–777. https://doi.org/10.1002/jemt.20968.

47. Wang, X., You, C., Hu, X., Zheng, Y., Li, Q., Feng, Z., Sun, H., Gao, C., and Han, C. (2013). The roles of knitted mesh-reinforced collagen-chitosan hybrid scaffold in the one-step repair of full-thickness skin defects in rats. Acta Biomater. *9*, 7822–7832. https://doi.org/10.1016/j.actbio.2013.04.017.

48. Veith, A.P., Henderson, K., Spencer, A., Sligar, A.D., and Baker, A.B. (2019). Therapeutic strategies for enhancing angiogenesis in wound healing. Adv. Drug Deliv. Rev. *146*, 97–125. https://doi.org/10.1016/j.addr.2018.09.010.

49. Shahin, H., Elmasry, M., Steinvall, I., Söberg, F., and El-Serafi, A. (2020). Vascularization is the next challenge for skin tissue engineering as a solution for burn management. Burns Trauma *8*, tkaa022. https://doi.org/10.1093/burnst/tkaa022.

50. Tai, Y., Woods, E.L., Dally, J., Kong, D., Steadman, R., Moseley, R., and Midgley, A.C. (2021). Myofibroblasts: function, formation, and scope of molecular therapies for skin fibrosis. Biomolecules *11*, 1095. https://doi.org/10.3390/biom11081095.

51. Shao, P.L., Liao, J.D., Wu, S.C., Chen, Y.H., and Wong, T.W. (2021). Microplasma treatment versus negative pressure therapy for promoting wound healing in diabetic mice. Int. J. Mol. Sci. *22*, 10266. https://doi.org/10.3390/ijms221910266.

52. Crawford, L., Wyatt, M., Bryers, J., and Ratner, B. (2021). Biocompatibility evolves: phenomenology to toxicology to regeneration. Adv. Healthc. Mater. *10*, e2002153. https://doi.org/10.1002/adhm.202002153.

53. Elbialy, Z.I., Assar, D.H., Abdelnaby, A., Asa, S.A., Abdelhiee, E.Y., Ibrahim, S.S., Abdel-Daim, M.M., Almeer, R., and Atiba, A. (2021). Healing potential of Spirulina platensis for skin wounds by modulating bFGF, VEGF, TGF-ß1 and α-SMA genes expression targeting angiogenesis and scar tissue formation in the rat model. Biomed. Pharmacother. *137*, 111349. https://doi.org/10.1016/j.biopha.2021.111349.

54. Jetten, N., Verbruggen, S., Gijbels, M.J., Post, M.J., De Winther, M.P.J., and Donners, M.M.P.C. (2014). Anti-inflammatory M2, but not pro-inflammatory M1 macrophages promote angiogenesis in vivo. Angiogenesis *17*, 109–118. https://doi.org/10.1007/s10456-013-9381-6.

55. Kovalchuk, V., Voronkina, A., Binnewerg, B., Schubert, M., Muzychka, L., Wysokowski, M., Tsurkan, M.V., Bechmann, N., Petrenko, I., Fursov, A., et al. (2019). Naturally drug-loaded chitin: isolation and applications. Mar. Drugs *17*, 574. https://doi.org/10.3390/md17100574.

56. Xie, X., Li, D., Chen, Y., Shen, Y., Yu, F., Wang, W., Yuan, Z., Morsi, Y., Wu, J., and Mo, X. (2021). Conjugate electrospun 3D gelatin nanofiber sponge for rapid hemostasis. Adv. Healthc. Mater. *10*, e2100918. https://doi.org/10.1002/adhm.202100918.

57. Hao, W., Han, J., Chu, Y., Huang, L., Zhuang, Y., Sun, J., Li, X., Zhao, Y., Chen, Y., and Dai, J. (2018). Collagen/heparin Bi-affinity multilayer modified collagen scaffolds for controlled bFGF release to improve angiogenesis in vivo. Macromol. Biosci. *18*, e1800086. https://doi.org/10.1002/mabi.201800086.

58. Liang, Y., Zhao, X., Hu, T., Chen, B., Yin, Z., Ma, P.X., and Guo, B. (2019). Adhesive hemostatic conducting injectable composite hydrogels with sustained drug release and photothermal antibacterial activity to promote full-thickness skin regeneration during wound healing. Small *15*, e1900046. https://doi.org/10.1002/smll.201900046.

59. He, Y., Xia, J., Chen, H., Wang, L., Deng, C., and Lu, F. (2019). Human adipose liquid extract induces angiogenesis and adipogenesis: a novel cell-free therapeutic agent. Stem Cell Res. Ther. *10*, 252. https://doi.org/10.1186/s13287-019-1356-0.

STAR★METHODS

KEY RESOURCES TABLE

REAGENT or RESOURCE	SOURCE	IDENTIFIER
Chemicals, peptides, and recombinant proteins		
Chitosan low molecular weight	Macklin	CAS:9012-76-4
Acetic acid	aladdin	CAS:64-19-7
Heparin sodium	Macklin	CAS:9041-08-1
N-hydroxysuccinimide (NHS)	Macklin	CAS:6066-82-6
N-(3-Dimethylaminopropyl)-N′- ethylcarbodiimide (EDC)	Macklin	CAS:1892-57-5
Cell Counting Kit-8(CCK8)	DOJINDO	CAS:CK04-500T
Porcine platelet-derived growth factor, PDGF ELISA	MEIMIAN	CAS:MM-0484O2
Porcine vascular endothelial cell growth factor, VEGF ELISA	Andygene	CAS:AD0069Po
Dopamine (hydrochloride)	Solarbio	CAS:D806618-500g
Trimethylaminomethane (TRIS)	Macklin	CAS:T818967-100g
Deoxyribonucleic acid (DNA) test kit	HKHCBIO	CAS:C11724
Rhodamine-Phalloidin	Solarbio	CAS:CA1610-300T
DAPI dye solution	Beyotime	CAS:C1006
Calcein -AM/PI live/dead staining kit	YOBIBIO	CAS:U23-002A
Antibodies		
a-SMA monoclonal antibody	Bioss	CAS:bsm-33187M-100ul
KI67 Cell Proliferation Kit	BBI	CAS:E607238-0100
CD31 antibody	FineTest	CAS:FNab01464
Bacterial and virus strains		
Gram-positive *Staphylococcus aureus*	ATCC	ATCC 27735
Gram-negative *Escherichia coli*	ATCC	ATCC 8099
Experimental models: Cell lines		
Immortalized human dermal keratinocytes (HaCaT)	MEISENCTCC	CTCC-0383-Luc1
Human umbilical vein endothelial cells(HUVEC)	iCell	iCell-0050a
Mouse fibroblasts (L929 Cells)	NEWGAINBIO	CM3075
Software and algorithms		
ImageJ	National Institutes of Health, USA	
SPSS version 23.0	IBM Corporation	
GraphPad 8.02	GraphPad Software, USA	

RESOURCE AVAILABILITY

Lead contact

Further information and requests for resources and reagents should be directed to and will be fulfilled by the lead contact, Prof. Lianglong Chen (chen18379797486@163.com).

Materials availability

This study did not generate new unique reagents.

Data and code availability

- All data reported in this work will be shared by the lead contact upon reasonable request.
- This work has no original code and custom computer code.

- Any additional information required to reanalyze the data reported in this work is available from the lead contact upon request.

EXPERIMENTAL MODEL AND SUBJECT DETAILS

Cell lines

Mouse fibroblasts (L929 Cells),Immortalized human dermal keratinocytes (HaCaT) and Human umbilical vein endothelial cells(HUVEC) grown under standard culture conditions (i.e. in a humidified atmosphere with 5% CO_2 at 37°C) in DMEM supplemented with 10% FBS, 0.1 mM NEAA, 2 mM L-Glutamine, 1 mM sodium pyruvate, and 1% penicillin-streptomycin, respectively.

METHOD DETAILS

Preparation of an acellular dermal matrix-chitosan composite sponge scaffold

The acellular dermal matrix was prepared by the hypertonic salt-alkali method using the full-thickness skin of white Tibetan miniature pigs as raw material. The solutions containing 0.5%, 1%, and 2% acetic acid were designed. The PADMS and acetic acid solutions were added in a mass ratio of 1:10. In a beaker, stirred at 1500 rpm for 48 hours, filtered to form an acellular dermal matrix gel (group marked as 0.5%, 1%, and 2%), and stored at 4°C for later use. Acellular dermal matrix gel (group marked as 10% PADM) was mixed with 3% chitosan (deacetylation degree ≥95%, viscosity 100~200 Mpa.s, Macklin) solution in different volumes ratios (group marked as CADMS) and cross-linked with glutaraldehyde solution. The acellular dermal matrix-chitosan composite gel was prepared with a 0.02 V/v.% cross-linking agent (group labeled as CADMS-G). The prepared acellular dermal matrix-chitosan composite gels (groups marked as 1:1, 1:2, 1:3, 1:4, 1:5, 1:6, 2:1, 3:1, 4:1, 5:1). The above gel was freeze-dried to prepare a composite sponge scaffold, soaked in a 70% ethanol solution for 1 hour to remove residual acetic acid, thoroughly washed, and then freeze-dried again for subsequent characterization of physical and chemical properties.

Preparation of heparin sodium modified composite sponge scaffold

EDC and NHS were added to 0.1 mol/L MES buffer, and the final concentrations were 2 g/L and 0.5 g/L, respectively, with pH=5.0. Heparin was added to the prepared reaction solution, and the reaction time was 20 min. The lyophilized acellular dermal matrix chitosan composite sponge was added to the ready reaction solution for 24 h at room temperature, followed by washing with 0.1 mol/L PBS buffer for 1 h, and finally washed with deionized water three times for 30 min each, followed by freeze-drying for backup (labeled group CADMS-G-Hep).

Preparation of composite sponge scaffolds doped with polydopamine nanosphere

The specific experimental method is as follows: Firstly, ammonia water (0.8 mL, 28~30%), anhydrous ethanol (40 mL), and deionized water (90 mL) are stirred and mixed evenly. Dopamine HCl (0.5 g) was dissolved in distilled water (10 mL), and the dopamine HCl solution was added drop by drop to the above mixture. The dopamine powder (0.5 g) was dissolved in distilled water (10 mL), and the dopamine hydrochloride solution was added drop by drop to the mixture. Polydopamine nanoparticles (PDA-NPS) were obtained by stirring for 30 h and centrifugation at 10,000 RPM for 15 min. PDA-NPS was washed with distilled water three times and freeze-dried for later use. Composite sponge scaffolds with 1 g/L, 2 g/L, and 4 g/L were prepared by adding PDA-NPS into 10 mL of acellular dermal matrix-chitosan mixed gel (groups were labeled as CADMS-G-1-Hep, CADMS-G-2-Hep, and CADMS-G-4-Hep, respectively).

Preparation of concentrated growth factor delivery sustained-release scaffold

The healthy male white Tibetan miniature pigs weighing about 40 kg were anesthetized with isoflurane gas. The Animal Experimentation Ethics Committee approved this study at Nan fang Hospital, Southern Medical University, China. White Tibetan miniature pigs (n = 3, 6 months old, weighing 40 kg) were purchased from the laboratory animal center of Southern Medical University. The whole blood was collected from the internal jugular vein and distributed to the anticoagulant-collecting vessels containing sodium meerkats. The blood was gently rotated, mixed, and centrifuged in a CGF centrifuge for about 14 minutes to obtain the supernatant CGF solution. After irradiation sterilization of Co^{57}, the composite sponge scaffold was soaked in CGF solution for 1 h so that the growth factors were fully adsorbed on the sponge scaffold. Finally, the sponge drug delivery scaffold (group labeled as CADMS-G-2-Hep-CGF) was obtained.

Physical and chemical properties characterization of materials

Fourier infrared and Raman spectroscopy

The sample and potassium bromide are mixed and ground into 0.1% ~ 0.5% powder. Then, the tablet is pressed and determined by the infrared spectrometer. Infrared spectroscopy (Nicolet IS50FI-IR) detection range of 500 ~ 4000 cm^{-1}, resolution of 4 cm^{-1}. The authors thank Suzhou Deyo Bot Advanced Materials Co., Ltd. (www.dy-test.com) for supporting material characterization. The Raman spectrum of the sample at 400~2800 cm^{-1} was obtained by using a Raman spectrometer (Renishaw RM2000), 532 mm ion laser with a resolution of 1 cm^{-1}.

Scanning electron microscope

Round pieces of dry samples with diameters of 6mm in different proportions were glued to the test bench with a conductive adhesive. Gold spraying was carried out under vacuum by a sputtering machine under 1 kV and 5 mA conditions. Scanning electron microscopy (SEM; TM3030, HITACHI) observed the material's microstructure under 20 kV acceleration voltage.

Water absorption

Take an appropriate amount of scaffold material, weigh the mass as M1, immerse the sample in purified water and soak it at room temperature for 24 hours. After it absorbs enough water, remove and absorb the excess water on the material's surface. Weigh the wet mass as M_2, and calculate the water absorption using the following formula. Water absorption = $(M_2\text{-}M_1)/M_1 \times 100\ \%$。

Porosity

The centrifuge tube with a volume of 10 mL was filled with ethanol and weighed (denoted as W_1). The sample was weighed (denoted as W_S) and immersed in the ethanol-filled centrifuge. The sample was placed into the ultrasonic instrument for 30 min, filled with ethanol, and weighed (denoted as W_2). After the sample was filled with ethanol, the remaining ethanol and the centrifuge tube were weighed (W_3). The experiment was repeated three times, and the mean value was taken. Calculate the porosity = $(W_2\text{-}W_3\text{-}W_S)\ /(W_1\text{-}W_3) \times 100\%$.

Moisture retention

Accurately weigh the sample mass W_{dry} and immerse it in distilled water to make it fully absorb water and swell. Put it into the centrifuge tube at 500 r/min for 3 min, and take out the weighing W. Repeat the measurement three times in each group. Calculate the moisture retention of the material: WR = $(W\text{-}W_{dry})\ /\ W_{dry}$

Mechanical strength test

An electronic universal testing machine (UTM100, Wanchen) was selected to test the static mechanical properties of the samples in a dry state through the tensile test. First, different proportions of materials (n = 3) with a thickness of about 1.5 mm were cut into rectangular samples with specifications of 4 × 1 cm. The loading rate was 10 mm/min, and the elastic modulus calculation formula: $E = \sigma/\varepsilon$. E is the elastic modulus, σ is the stress, and ε is the strain.

Determination of residual dsDNA

Deoxyribonucleic acid (DNA) was extracted from PADMS using a DNA kit (Tiangen Biotech(Beijing) CO., LTD DP304). The residual DNA content was then measured with an ultramicro spectrophotometer (Thermo, NanoDrop2000) and normalized to the dry weight of each sample.

In vitro degradation experiment

The samples were placed in a 15mL centrifuge tube, and 4 mL of 50 mg/mL type I collagenase (Solarbio, China) solution was added and taken out at six-time points (n=3) at 2 h, 4 h, 12 h, 16 h, 21 h, and 24 h. After freeze-drying, the samples were weighed. The degradation rate was calculated according to the quality difference before and after degradation.

In vivo degradation experiment

Male SD rats aged 12 weeks were anesthetized with 0.03 % pentobarbital sodium, the sample (diameter 12 mm, thickness about 2 mm) was implanted subcutaneously, and the wound surface was sutured discontinuously. Photographs were taken at 2, 6, 8, and 16 weeks, and H&E staining was performed.

Toluidine blue staining

The toluidine blue staining solution was diluted to 10%, and the materials were put into the toluidine blue staining solution dyeing VAT and soaked for 20~30 min. After the staining, the materials were removed, and the tissues were thoroughly washed with deionized water. The absorbance of OD^{600} was measured by direct photographing or an enzyme-plate meter.

Composite bracket NIR photothermal properties

Will have the same size (diameter: 10 mm, height: 10 mm); samples were placed in 2 mL distilled water and irradiated with 808 nm NIR laser (0.8 W cm^{-2}) for 30 min. The water temperature was measured and recorded with a thermometer every 5 min. An infrared thermal imager (XINTEST, China) photographed the temperature distribution around the composite scaffold at different time points.

In vitro antibacterial test

The plate method was used to quantitatively evaluate the *in vitro* antibacterial activity of composite sponge scaffold against Gram-positive *Staphylococcus aureus* (ATCC 27735) and Gram-negative *Escherichia coli* (ATCC 8099). The bacteria were cultured in a standard Luria-Bertani (LB) medium. Each group's materials were incubated with 200 μL bacterial suspension in 48-well plates for 24 h. After ultrasonic cleaning for 15 min, 10 μL of the appropriate diluted bacterial solution was placed on Columbia blood AGAR, incubated at 37°C for 36 h, and colonies were counted. Antibacterial Rate (%) = $\frac{(C-M)}{C} \times 100\%$, in the formula, C and M are the number of bacteria (CFUs) in the control group and material group respectively. Each experiment was repeated at least three times. Statistical significance of the data obtained by calculating p-value analysis.

Histomorphological staining

Different materials were fixed with paraformaldehyde (Aladdin, China), dehydrated by an automatic dehydrator, embedded in paraffin, and then paraffin sectioning. After dewaxing, hematoxylin-eosin staining, Masson staining, and toluidine blue staining were performed.

Growth factor release experiment

The compound sponge drug delivery stent (CADMS-G-2-Hep-CGF) was immersed in PBS buffer (Sigma-Aldrich, USA). The supernatant was rapidly absorbed at room temperature at 2, 12, 24, 36, 48, 60, and 72 h. The release curves of VEGF and PDGF-BB were quantitatively determined using an Enzyme-Linked immunosorbent assay (ELISA) kit. The materials' sustained-release drug loading characteristics were evaluated, repeating each experiment at least three times.

Cytotoxicity test

The material was immersed in a complete medium at 37°C for 24 h to prepare the extract and inoculated into 96-well plates at 2×10^4 cells/mL density. That was inoculated into After cell adherence, quotes were added, and a blank control group was used as the basal medium. A cck-8 reagent solution (DOJINDO, Japan) was added for 48 h and incubated at 37°C for 1 h. Optical density values of each well (D) were measured at 450 nm wavelength by BioTek (China), and the measured data were statistically analyzed (n=3). Alternatively, the morphology of HaCat was photographed under a microscope at 36h. The basal medium was used to dilute CGF to 5%, 10%, 15%, 20%, and 25%, and the control group was a 10% complete medium. L929 cells were inoculated into 24-well plates at a density of 3×10^4 cells/mL, and cell morphology was photographed under a microscope at 24 h, 36 h, 48 h, and 60 h, respectively.

Scratch test

L929 cells/HUVEC were inoculated into 6-well plates at a rate of 5×10^5 cells/well (n = 3) and cultured in an incubator at 37°C until confluence. Then use the pipette tip to make a scratch at a constant speed on the cell layer on the back of the plate. After three washes with PBS, the 24 mm insert (micron microporous polyester film) was placed into the 6-well dish, and the material was transferred to the insert. Subsequently, serum-free medium was added to the orifice plate until the scaffold was immersed. Alternatively, different concentrations of CGF can be added to the 6-well plate. Cell migration was recorded at 0 h, 12 h, 20 h, 36 h, and 48 h, respectively. The migration area was calculated as follows: mobility (MR)(%)=$(R_0 - R_n)/R_0\times100\%$, where R_0 represents the initial scratch area and R_n represents the remaining unsealed scratch area.

Staining of living and dead cells

The staining solution was prepared from 10 uL of 1 mmol/L Calcein-AM reserve solution and 15uL of 1.5 mmol/L PI reserve solution (Solarbio, China) to 5 mL of PBS and frozen at 0°C under dark conditions for later use. Three days after HUVEC/L929 cells were inoculated into the material, the original medium was dried, and the material was immersed entirely with 100 uL of PI/CA staining solution. The staining solution was washed with normal saline in the cell incubator for 20 min, and the inverted fluorescence microscope (Axio Observer D1, ZEISS, Germany) images of cell proliferation and adhesion at 490 nm were obtained to observe the number and state of cells. The experiment was repeated with three samples in each group.

Cell proliferation and adhesion experiments

HUVEC was inoculated on each group of 96-well plates at a density of 10^5 cells/mL and cultured at 37°C with a medium exchange culture every two days. On day 3 of the culture, the samples were removed from the incubator, washed with PBS, and fixed with 4% paraformaldehyde at room temperature. Then the fixation solution was washed away with PBS, and the cells were sequentially permeated with 0.1% Triton X-100 and 1% bovine serum albumin. According to the manufacturer's agreement, the cytoskeleton and nucleus were subsequently stained in a dark chamber with Rhodamine-labeled Phalloidin and 4, 6-Diamidino-2-phenylindole (DAPI) solution (Abcam), respectively. Finally, laser scanning confocal microscopy (LSM 880, ZEISS, Germany) was used to obtain cell proliferation and adhesion images at 405/516 nm, recording three field images per sample.

In vivo wound healing in a full-layer skin model

According to the ethical standards of the International Center for Animal Experiments, this study was approved by the Ethical Committee for Animal Experiments of Nanfang Hospital, Southern Medical University, China. Male SD rats (n = 48, 12 weeks of age, 250∼270 g) were purchased from the experimental animal center of Southern Medical University. Before the experiment, 0.03 % pentobarbital sodium (0.2 ml/ 10 g) was used to induce anesthesia after one week of environmental adaptation. Under the condition of aseptic surgery, full-thickness skin defect wounds of 12 mm in diameter were made on both sides of the back. The animals were randomly divided into four groups: CADMS-G-2-Hep-CGF, CADMS-G-2-Hep, CADMS-G, and normal saline (NS, as blank control). The full-thickness skin piece is then used to optimize material into two wound beds, with a continuous suture of full-thickness skin cover, finally to disinfect the wound, and in turn with vaseline gauze, sterile dressings, pressurized packaging, external dressing change once every three days, and 14 days to dismantle dressings. 12 rats were killed by carbon dioxide inhalation on days 7, 14, 21, and 28 after surgery (24 wounds in total, 6 times in each group). At the same time, rats' hearts, livers, spleens, lungs, and kidneys were collected. Then all the samples were fixed with paraformaldehyde, embedded in paraffin, and stained for subsequent experimental operations.

Male SD rats (n = 8,12 weeks old, weighing 250∼270g) were purchased from the laboratory animal center of southern medical university and performed as described above during the perioperative period. Under aseptic surgical conditions, 4 full-thickness skin defect wounds with a diameter of 12 mm were created on both sides of the back. The animals were randomly divided into four groups: non-NIR stimulation group (CADMS-G-2-Hep-CGF, CADMS-G-2-Hep) and NIR stimulation group (CADMS-G-2-Hep-CGF-INR and CADMS-G-2-Hep-INR). In the non-NIR stimulation group, no NIR light was used, while in the NIR stimulation group, the back of SD rats was irradiated with NIR light (0.05∼0.1 W cm^{-2}) for 30 min every day. The wound area of rats was recorded at 0,3,7,14 and 21 days. SD rats were sacrificed on the 14th and 28th days (32 wounds in total, 4 replicates in each group). For subsequent experimental operations, the tissues around the implanted samples were removed for fixation, embedding, and sectioning.

Skin graft survival, contraction, and capillary density

The wound was photographed with a digital camera, and the unhealed and scarred areas were quantified by Image J software. The graft and surrounding tissue were collected and flattened on a transparent petri dish. A white light source was set up from the bottom of the word to illuminate the sample, observe the blood vessels, and photograph and record them. The difference in skin contraction was calculated relative to the skin wound/graft size using a gravity-plane measurement. Shrinkage rate = [1- (Fancied area size/ Original Wound size)] ×100%.

H&E and Masson trichromatic staining

Paraffin-embedded samples were secularized and dewaxed, followed by hematoxylin and eosin (H&E) staining and Masson trichromatic staining. Images were taken using an automatic section scanner (C10730-12, HAMAMATSU), and collagen density was measured using Image J software. Capillaries were counted in 3 areas of each H&E section by two blind inspectors, who assessed the vascularization of the samples.

Immunohistochemical staining of Ki67, CD31, and α-SMA

Immunohistochemistry of Ki67, CD31, and α-SMA was used to evaluate tissue regeneration, angiogenesis, and scar formation in wound tissue, respectively. In short, the skin tissues of each group were routinely dewaxed, repaired, washed, sealed, diluted, cleaned, incubated with antibodies, stained, and sealed, and then photographed with a fluorescence microscope or automatic sectioning scanner.

Proteomic analysis

In this study, a series of cutting-edge technologies, including protein extraction, enzyme digestion, liquid chromatography-mass spectrometry tandem analysis, and bio information analysis, were organically combined to study the quantitative proteome of white Tibetan miniature pig skin and acellular dermal matrix sponge samples. The peptides were isolated using an EASY-NLC 1200 ULTRA-high Performance liquid chromatography system. The peptides were separated by an ULTRA-high-performance liquid chromatography system and injected into an NSI ion source for ionization and analysis by Orbitrap Exploris^{TM} 480 mass spectrometry. Proteome Discoverer (V2.4.1.15) was used to retrieve secondary mass spectrometry data in this experiment. The database was Blast_Sus_scrofa_9823_PR_20210806. Fasta (49792 sequences). A counter library was added to calculate the false positive rate (FDR) due to random matching. A shared contamination library was added to the database to eliminate the influence of toxic proteins in the identification results.

Statistical analysis

All quantitative data were recorded with SPSS software (version 23.0, IBM Corporation) and presented as mean ± standard deviation. Statistical comparisons between groups were performed using Independent Student's t-test or one-way ANOVA when appropriate. All quantitative data were recorded with GraphPad 8.02 software. Values of $P < 0.05$ (*) and $P < 0.01$ (**) were considered statistically significant, and ns indicated not substantial.